



ELSEVIER

Marine Geology xx (2007) xxx–xxx

**MARINE
GEOLOGY**
INTERNATIONAL JOURNAL OF MARINE
GEOLOGY, GEOCHEMISTRY AND GEOPHYSICS

www.elsevier.com/locate/margeo

Origin of continental margin morphology: Submarine-slide or downslope current-controlled bedforms, a rock magnetic approach

K. Schwehr*, N. Driscoll, L. Tauxe

Scripps Institution of Oceanography, University of California San Diego, San Diego, CA 92093-2002, USA

Received 24 March 2006; received in revised form 24 January 2007; accepted 31 January 2007

Abstract

Morphological features observed in both swath bathymetry and seismic reflection data are not unique, which introduces uncertainty as to their origin. The origin of features observed in the Humboldt Slide has generated much controversy because the same features have been interpreted as a submarine failure deposit versus current-controlled sediment waves. It is important to resolve this controversy because similar structures are observed on many continental margins and the origin of these features needs to be understood. Anisotropy of magnetic susceptibility (AMS) measurements on sediment samples acquired from the Humboldt Slide reveal that the top ~ 8 m have not experienced post-depositional deformation. This suggests that these features are formed by primary deposition associated with downslope currents. Using the same AMS technique on a core acquired north of the Humboldt Slide in a region with no geophysical evidence for post-depositional deformation, we were able to identify a ~ 1 m thick deposit that appears to be a small slump.

© 2007 Elsevier B.V. All rights reserved.

Keywords: submarine landslides; slope failure; anisotropy of magnetic susceptibility; STRATAFORM; Humboldt Slide; Eel River Basin

1. Introduction

Geologists have long appreciated the importance of submarine landslides and failures in the development of unconformities (Embley and Jacobi, 1986; Booth et al., 1993; Evans et al., 1996). Recently there has been much debate concerning the identification of submarine landslides and rotational slumps in seismic reflection data (Dillon et al., 1993; Gardner et al., 1999; Holbrook, 2001; Holbrook et al., 2002; Lee et al., 2002; Trincardi et al., 2004). The controversy arises, in large part, because the stratal geometry of many deposits, previously identified as retrogressive slumps, is not unique and could equally

be generated from down- or along-slope currents (e.g. Blake–Bahama collapse structure, Holbrook et al., 2002; Humboldt Slide in the Eel River Basin, Fig. 1).

Deposition and erosion of the slope may be caused by a number of different processes (e.g., slope failure, incision and overbank deposits, bottom currents, shelf-edge deltas). Understanding how these processes sculpt the continental slope is critical to generating quantitative geologic models of continental slope evolution (Pratson and Coakley, 1996; Driscoll and Diebold, 1999). Developing a test to discriminate between these alternative scenarios, retrogressive slumps versus current-controlled deposits, would provide valuable new insights into the origin of these deposits and their relative importance in the construction and evolution of continental margins.

* Corresponding author.

E-mail address: kurt@ccom.unh.edu (K. Schwehr).

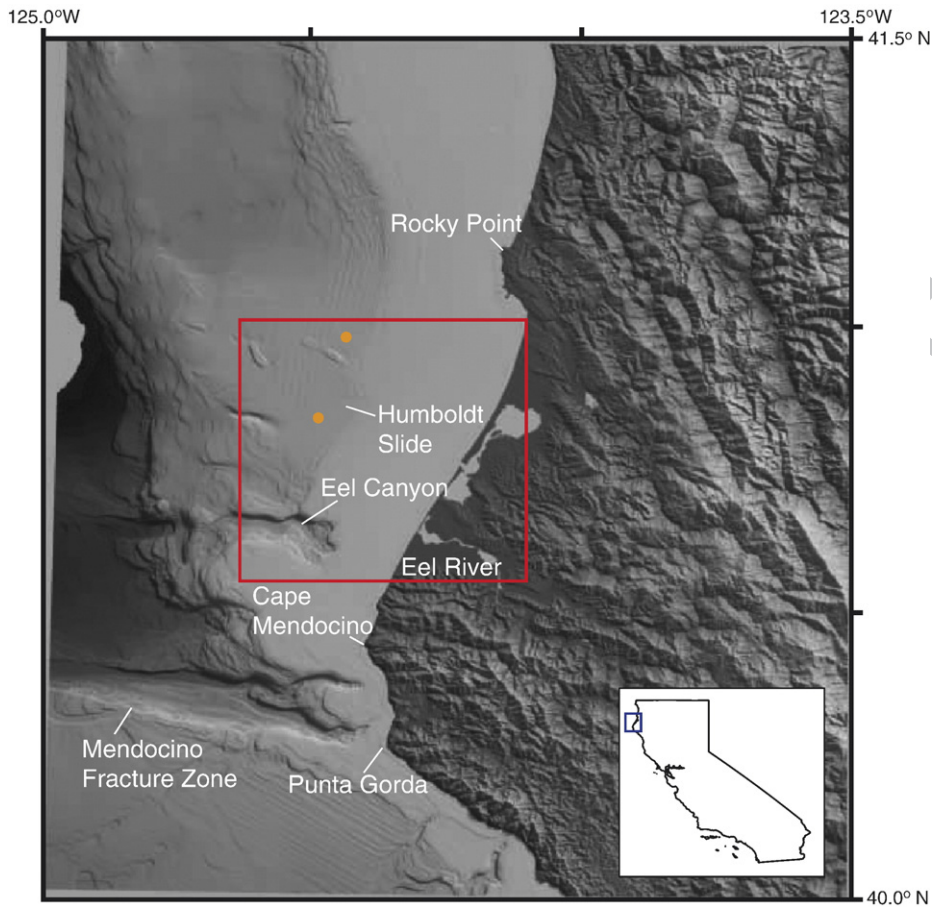


Fig. 1. The Eel River Basin is located in northern California, just north of the Mendocino Triple Junction. The Eel River enters the ocean south of Humboldt Bay. The slide is bounded by the Little Salmon Fault Zone to the north, the Eel Canyon to the south and up dip is delineated by the shelf break. The bathymetry is a compilation of the STRATAFORM EM1000, MBARI EM300 and the NOAA coastal relief 3 second data. The red inset shows the location of the study area (Fig. 2) with the core locations marked with orange circles.

49 Gardner et al. (1999) interpret the Humboldt Slide as
 50 having been formed by retrogressive failure and rotation
 51 of blocks above a shear zone. Lee et al. (2002)
 52 reinterpreted the Humboldt Slide complex as sediment
 53 waves emplaced by downslope gravity flows and argued
 54 that sediment waves are infilling a slide scar. The dif-
 55 fering interpretations of the structure by Gardner et al.
 56 (1999) and Lee et al. (2002) highlight the ongoing
 57 controversy regarding the origin of this type of morpho-
 58 logical feature around the globe (of which the Humboldt
 59 Slide complex is only one such example). These two
 60 interpretations (primary depositional features versus
 61 retrogressive faulting and internal deformation) are
 62 based on the same Huntec (Dodds, 1980) seismic data set.

63 The difficulties of interpreting such structures are
 64 illustrated by the Blake–Bahama outer ridge. Holbrook
 65 (2001) reinterpreted existing USGS data from the
 66 Blake–Bahama outer ridge and refined the previous

67 interpretation of Dillon et al. (1993) that the observed
 68 features were normal faults associated with a gas-hydrate
 69 collapse structure. By examining the stratal geometry,
 70 Holbrook (2001) suggested the structures were growth
 71 faults recording several events, not just one event as
 72 suggested by Dillon et al. (1993). Subsequently, Holbrook
 73 et al. (2002) conducted an expensive 3D seismic survey to
 74 define the nature of the collapse structures. After ac-
 75 quiring the seismic data set, Holbrook et al. (2002) con-
 76 cluded that the features were in fact not growth faults, but
 77 were actually sediment waves.

78 In this paper, we apply a test based on sedimentary
 79 fabric as characterized by anisotropy of magnetic suscep-
 80 tibility (AMS) for assessing the origin of these ambiguous
 81 features of the Humboldt Slide. The test is based on
 82 magnetic fabrics to determine the extent of post-deposi-
 83 tional deformation, a prediction of the retrogressive failure
 84 hypothesis. We will outline and describe the results.

85 **2. Geologic setting**

86 The ongoing deformation, uplift, and erosion of the
 87 Californian hinterland provide vast amounts of sediment
 88 to the U.S. Pacific continental margin (Clarke, 1987;
 89 Field and Barber, 1993). The relatively high rate of
 90 sedimentation and recurrence of earthquakes (Couch,
 91 1980) makes the Eel River Basin an ideal locale to
 92 examine slope failure and consequent slide deposits. In
 93 addition to strong forcing functions, vast amounts of
 94 data have been acquired in the Eel Basin as part of the
 95 ONR STRATAFORM project (Nittrouer, 1999). This
 96 background allows us to place our results into a well-
 97 defined geological framework.

98 The Humboldt Slide deposit mantles a bowl-shaped
 99 depression that extends from the outer shelf to the middle
 100 slope on the Eel Margin (Fig. 2). On the basis of the
 101 internal geometry and surficial morphology of the
 102 Humboldt Slide deposit, two competing hypotheses
 103 have emerged: (1) The Humboldt Slide deposit and
 104 internal geometry were formed by retrogressive failure
 105 and rotation above a shear zone (detachment) with mini-

mal lateral translation of the deformed sediment carapace
 (Gardner et al., 1999), and (2) The deposit records pri-
 mary deposition by density currents (hyperpycnal flows)
 cascading down a pre-existing slide scar (Lee et al., 2002).
 In the primary deposition scenario, previous slope failure
 and evacuation of the failed material over-steepened the
 local slope and created the Humboldt Slide scar. Acceler-
 ation of the density flows in response to the locally over-
 steepened slope gives rise to current-controlled bedforms
 in this region.

The Eel River Basin has a narrow shelf (22 km from
 the Eel River to the shelf break above the Humboldt
 Slide) such that sediment can potentially escape over the
 shelf break onto the shelf slope and beyond (Alexander
 and Simoneau, 1999). The typical winter swell can re-
 suspend sand in 50–80 m of water, whereas large storms
 can rework sand on the middle to outer shelf, and
 perhaps down to the upper slope (Alexander and
 Simoneau, 1999). Deposition rates derived from ^{210}Pb
 and ^{137}Cs reveal high sediment accumulation rates
 (SAR) on the shelf, and on the slope in the area of the
 Humboldt Slide (Alexander and Simoneau, 1999).

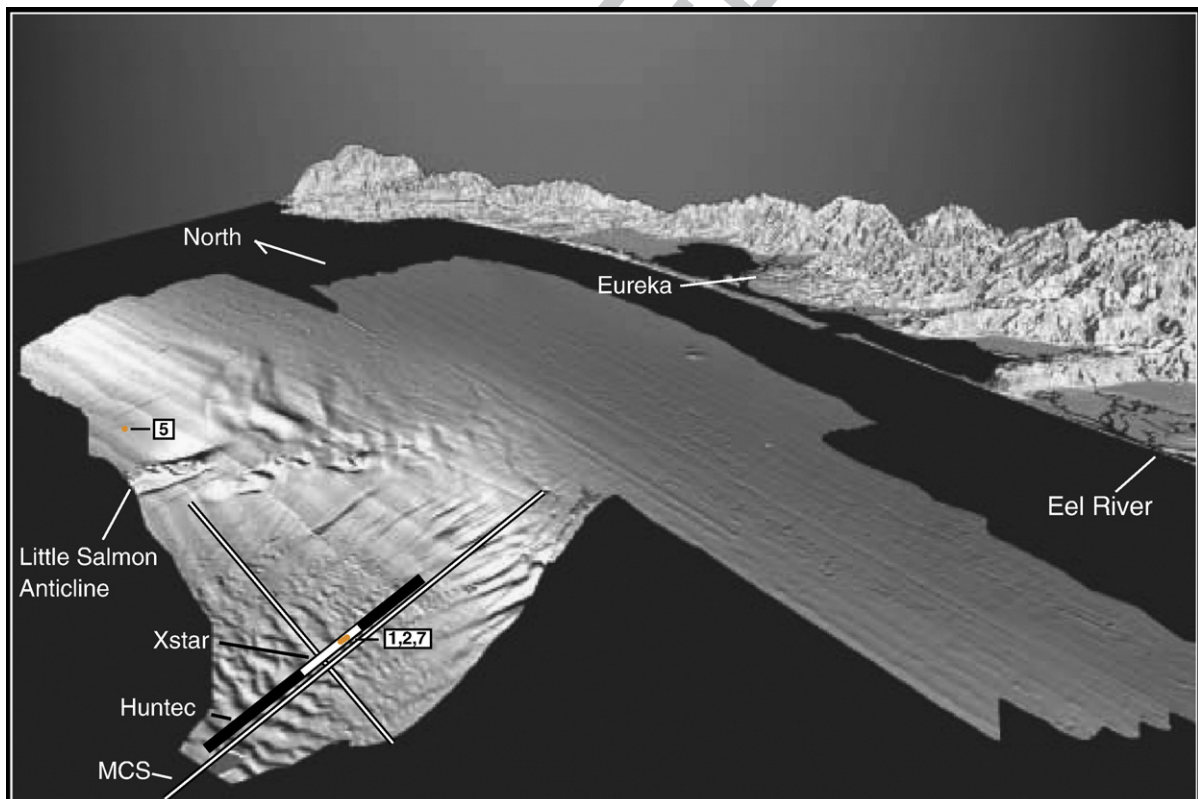


Fig. 2. Location of XStar CHIRP (Fig. 4), Hunttec (Fig. 5), and multi-channel seismic (MCS; Fig. 19) lines on the Humboldt Slide amphitheater. The core locations are marked with orange dots. Cores 1, 2 and 7 are coincident with the Chirp, Hunttec, and MCS E–W lines. Core 5, which was acquired outside of the Humboldt Slide, was used as a control core for the study. Image courtesy United States Geological Survey.

128 **3. Methods**129 **3.1. Sedimentary AMS fabrics**

130 Early workers such as Ising (1942), Rees (1961), and
 131 Marino and Ellwood (1978) suggested the use of AMS
 132 to test the reliability of natural remanent magnetism
 133 (NRM) measurements from sediments. From these
 134 measurements, they concluded that “normal” (oblate)
 135 AMS fabrics should generally yield robust results for
 136 paleomagnetic field studies. They found poor or
 137 incorrect results from samples that showed distorted
 138 magnetic fabrics and suggested a wide range of possible
 139 causes, including slumping.

140 Kanamatsu et al. (2001) summarized the potential
 141 ways that AMS fabric could be altered by internal

(mineralogical) changes and physical reorientation of
 142 magnetic grains. Internal changes may be from magne-
 143 tostriction, growth or dissolution, and brittle or plastic
 144 deformation of individual grains. Physical reorientation
 145 can be non-coaxial (simple) shear or compaction, which
 146 does not alter the fabric within each grain; however, the
 147 strain will still alter the overall magnetic fabric.
 148

A range of laboratory experiments have been con-
 149 ducted to examine the depositional controls on magnetic
 150 fabrics. For example, Rees and Woodall (1975) investi-
 151 gated a variety of materials using both running-water
 152 deposition and deposition from slurries slumping. The
 153 experimental results suggest a systematic variation in the
 154 AMS fabric with changes in the critical shear stress in the
 155 bottom boundary layer (i.e., increasing water current
 156 velocity). Additional experiments with plaster mixtures
 157

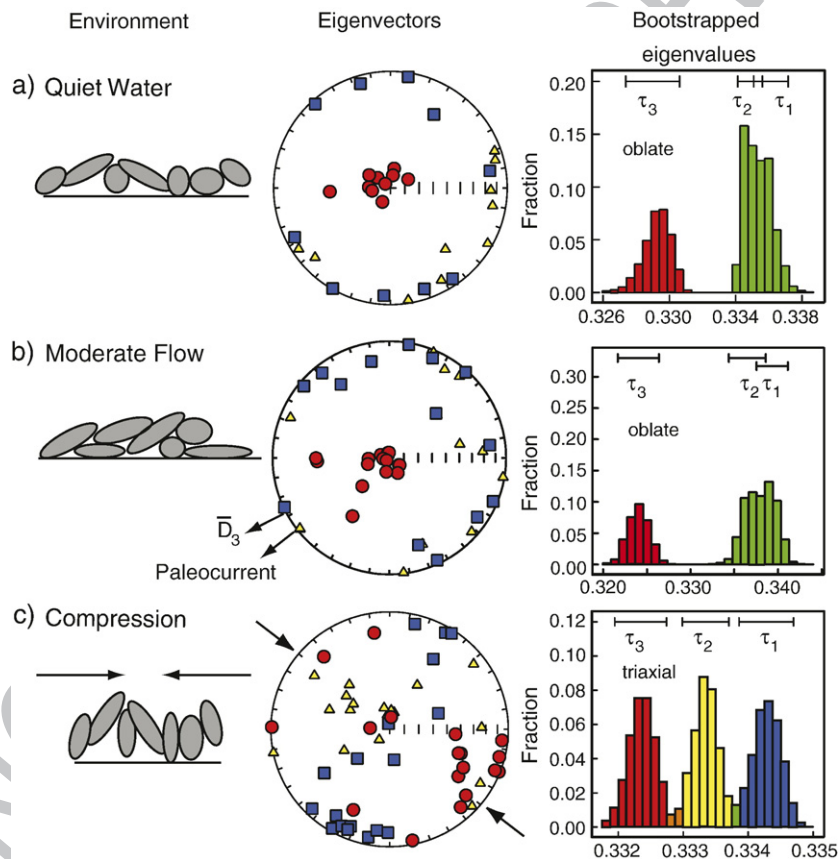


Fig. 3. Schematic diagram illustrating development of sedimentary magnetic anisotropy fabric. Eigenvector directions are plotted in the equal area projections whereby circles are the directions V_3 associated with the minimum eigenvalue τ_3 , triangles are V_2 associated with τ_2 and squares are the directions V_1 associated with the maximum eigenvalue τ_1 . The histograms to the right are bootstrapped eigenvalues for the specimens showing the 95% confidence intervals for τ_1 , τ_2 , τ_3 . a) Quiet water: the V_3 directions are typically vertical and τ_1 and τ_2 are not significantly different (i.e., the fabric is oblate). b) Moderate flow: the V_3 directions are deflected from the vertical by the current, but the fabric is still typically oblate. The bootstrap mean declination for V_3 (D^- sub 3) is the inferred direction of flow, which closely approximates the paleocurrent direction measured from ripples (Schwehr and Tauxe (2003)). c) Uniaxial horizontal deformation: the eigenvalues will be significantly different (i.e., the fabric is triaxial). In extreme cases, the V_3 directions will ultimately become horizontal. Arrows show the direction of compression that is orthogonal to the V_1 orientation. Note that scales vary for the histograms.

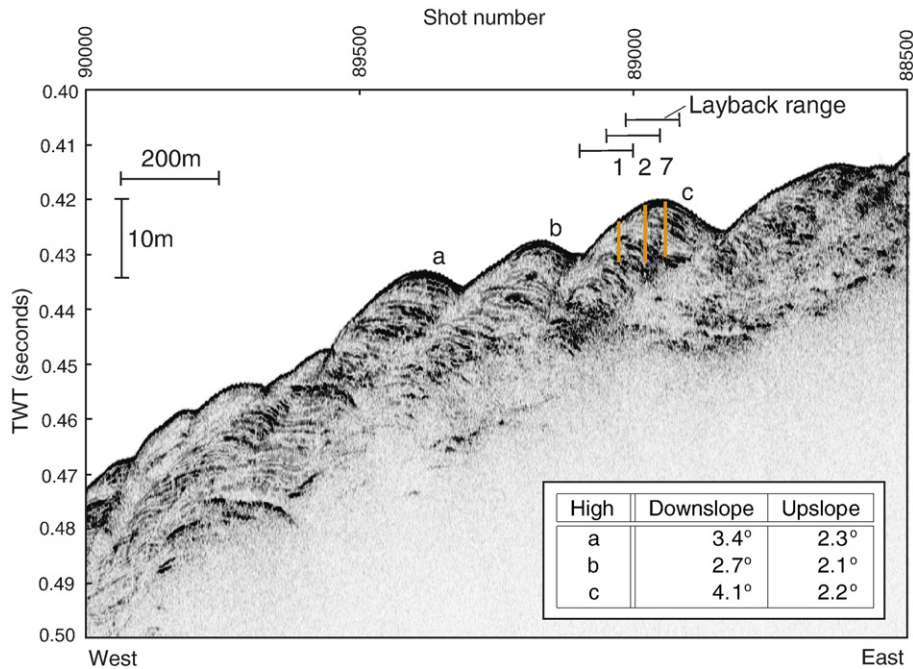


Fig. 4. EdgeTech XStar CHIRP seismic line collected in 1999 (See Fig. 2). This 1681 m long line trends NW–SE and images three prominent highs with internal reflectors (labeled a–c). Two way travel time is in seconds. Layback is calculated using wire angle and fish depth. The error bars are shown for wire angles ranging from 30 to 45° with the cores located at a wire angle of 35°, which is why the error bars are not symmetric with respect to the cores. The inset table shows the seafloor slopes of the three prominent highs that are labeled a–c on the CHIRP seismic line.

158 found that the eigenvector associated with the maximum
 159 eigenvalue can align either parallel or perpendicular to
 160 flow direction depending on flow conditions (Rees, 1983).
 161 Several authors have recognized the effects of sedi-
 162 ment deformation on NRM (see Tarling and Hrouda, 1993
 163 and Tauxe, 1998 for summaries). For example, Rosen-
 164 baum et al. (2000) examined a core (OL-92) from Owens
 165 Lake, CA that contains sediments ranging from 800 ka to
 166 the present. The original interpretation of the OL-92 mag-
 167 netic record was that there were a number of geomagnetic
 168 excursions in the Brunhes Chron (Glen and Coe, 1997).
 169 Rosenbaum et al. (2000) found that sediment deformation
 170 was associated with a number of these “excursions” and
 171 that the eigenvector associated with the minimum mag-
 172 netic susceptibility (here called V_3) could be used as an
 173 indicator for deformation. If the direction of V_3 is
 174 significantly deflected from vertical, that portion of the
 175 core might have been deformed, and therefore should not
 176 be used for field direction or field intensity. Rosenbaum
 177 et al. (2000) arrived at the conclusion that the deforma-
 178 tion observed in the OL-92 core was a result of fluid-
 179 ization. A seismic survey conducted after coring shows
 180 that the OL-92 core is located in the Owens Valley Fault
 181 Zone (Brooks and Johnson, 1997) and the deformation
 182 could have resulted from a combination of drilling and
 183 faulting.

184 Given that AMS is extremely sensitive to strain 184
 185 (Housen et al., 1996; Kanamatsu et al., 2001), magnetic 185
 186 fabric has recently been used to detect subtle deformation 186
 187 of sediments and to distinguish geomagnetic features 187
 188 from deformational artifacts (e.g., Rosenbaum et al., 188
 189 2000; Cronin et al., 2001). Cronin et al. (2001) suggested 189
 190 that AMS could be used to detect slumps not otherwise 190
 191 obvious from the geologic field evidence (so-called 191
 192 “crypto-slumps”, Schwehr and Tauxe, 2003). These 192
 193 studies show that AMS can distinguish between post- 193
 194 depositional deformation and primary depositional fea- 194
 195 tures. Although AMS has long been used to detect 195
 196 deformation in a variety of geological applications, our 196
 197 aim is to determine the geological origin of a continental 197
 198 margin deposit. AMS may provide a powerful method 198
 199 that can be used in a number of geological settings to 199
 200 detect post-depositional deformation where existing data 200
 201 are equivocal. 201

202 There is always the possibility that there might be 202
 203 complications in the AMS results caused by diagenetic 203
 204 effects on the magnetic mineralogy. Such changes can 204
 205 be detected using rock magnetic methods such as 205
 206 anhysteretic remanent magnetization (ARM), isother- 206
 207 mal remanent magnetization (IRM), low field bulk 207
 208 susceptibility (χ_{lf} or sometimes written just χ) and high 208
 209 field susceptibility χ_{hf} (e.g. Banerjee et al., 1981; King 209

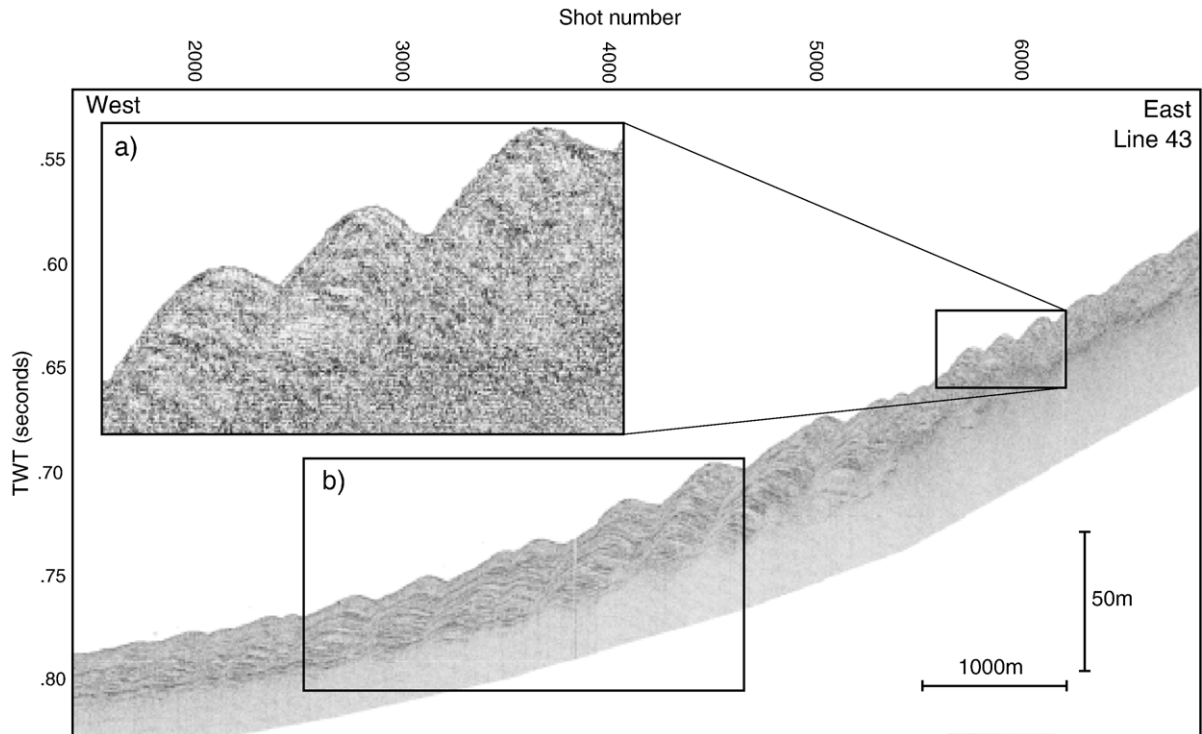


Fig. 5. Huntce seismic line collected in August 1995 on cruise W-2-95-NC. The line trends NW–SE across the structure and is from Gardner et al. (1999). Line 43 is 6086 m long, with the inset (region a) covering 910 m. Two way travel time is in seconds. Region a images the three structural highs that are shown in Fig. 4. Region b images a drape that is much thinner upslope in region a, the location of the cores (modified from Fig. 4 of Gardner et al., 1999).

210 et al., 1982; Karlin, 1990a; Leslie et al., 1990a; Tauxe
211 et al., 2002; Egli, 2004).

212 3.2. Development of magnetic fabric in sediments

213 Here we summarize decades of research on AMS
214 fabric in sediments in a variety of current regimes (see
215 Fig. 3; Tarling and Hrouda, 1993). In quiet water con-
216 ditions (Fig. 3a), there is a tendency for elongate par-
217 ticles to lie sub-parallel to the bedding plane. As the
218 magnetic susceptibility is usually at a maximum parallel
219 to the long axis of particles, the direction of maximum
220 magnetic susceptibility (V_1) will tend to lie close to the
221 plane of the bedding. However, there is no preferred
222 direction within the bedding plane, therefore the direc-
223 tion of intermediate magnetic susceptibility (V_2) and V_1
224 will be indistinguishable as will the associated eigen-
225 values (τ_2 and τ_1). Hence, the magnetic fabric will be
226 oblate with a vertical V_3 direction.

227 In moderate water currents (Fig. 3b), especially on
228 inclined bedding planes, particles may be slightly
229 deflected, resulting in off-vertical V_3 directions. Here
230 too, we expect the fabric to be characterized by an oblate

AMS ellipsoid, but the V_3 direction will be deflected in
the direction of the paleocurrent.

231
232
233 What happens to the magnetic fabric during post-
234 depositional deformation is more complex. Initial
235 theoretical work on the relationship between magnetic
236 fabrics and actual grain fabrics with respect to strain was
237 conducted by Owens (1974), Hrouda and Hruskova
238 (1990), and Housen et al. (1993). Most studies using
239 AMS fabric to determine strain have been applied on
240 tectonic scales and have examined weakly metamor-
241 phosed rocks (e.g. Pares et al., 1999; Kanamatsu et al.,
242 2001). Studies on such low-grade metamorphic rocks
243 are complicated because chemical changes during
244 metamorphism may affect the magnetic minerals to

Table 1

Cores 1, 2, and 7 were collected in the center of the Humboldt Slide

Core	Latitude	Longitude	Water depth (m)
1	124° 30' 09.96' W	40° 50' 20.16' N	460
2	124° 30' 07.62' W	40° 50' 19.86' N	460
5	124° 27' 12.08' W	40° 59' 00.30' N	419
7	124° 30' 05.84' W	40° 50' 19.87' N	461

Core 5 was collected to the north of the slide.

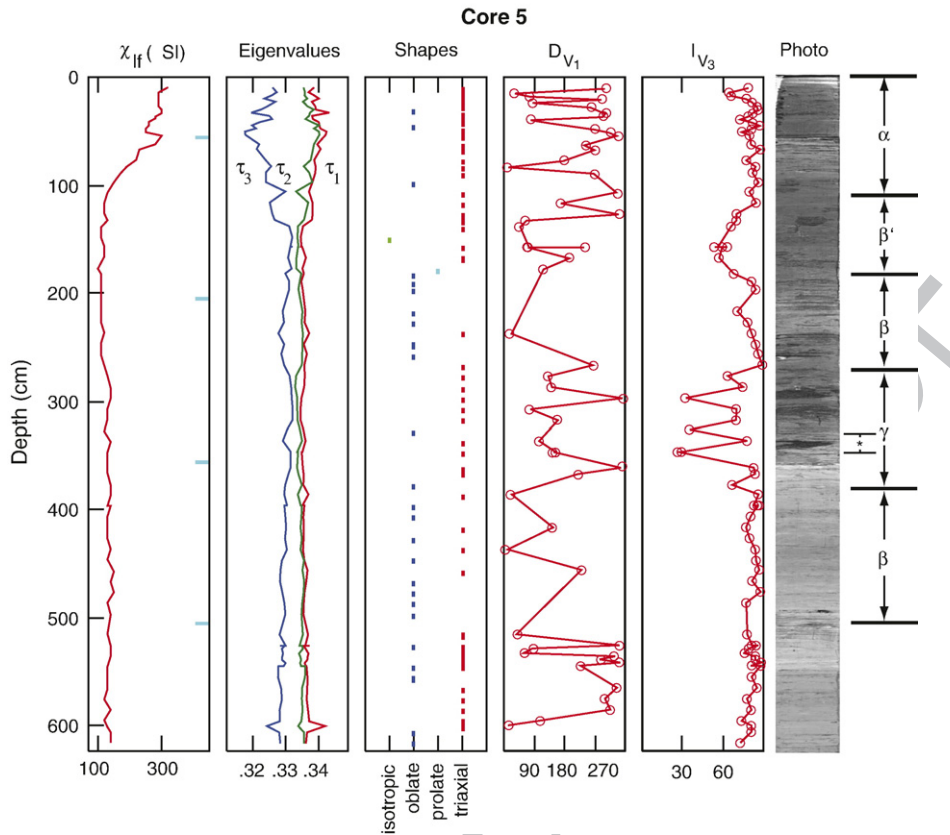


Fig. 6. Piston core 5 is located north of the Humboldt Slide as a control core. Down core measurements of bulk susceptibility (χ_{lf}), eigenvalues, fabric type (as illustrated in Fig. 3), D_{V1} (declination of the major eigenvector), and I_{V3} (inclination of the minor eigenvector) are shown. The majority of samples show triaxial fabric suggesting deposition under strong flow conditions. There is no systematic pattern in the D_{V1} , but there is a zone from 270 to 380 cm (γ zone) where I_{V3} differs significantly from vertical, which could possibly be a slump or extreme flow conditions. See Fig. 16 for an enlarged view of the region delineated by the (*) to the right of the core photo in the γ region, which appears to be a recumbent fold. The core photo shows that the γ region of shallow I_{V3} is located just above the transition from overlying darker sediment to the underlying lighter sediments. Vascular plants are concentrated in the upper darker regions. (For interpretation of the references to colour in this figure legend, the reader is referred to the web version of this article.)

245 some degree. It is difficult to separate physical from
 246 chemical effects on magnetic fabrics. Nonetheless, re-
 247 search shows that strain alters magnetic fabric and can
 248 have effects such as deflecting the minimum suscepti-
 249 bility vector from vertical, and aligning the maximum
 250 eigenvector perpendicular to the axis of compression
 251 (see Fig. 3c). By working with sediments that have not
 252 experienced diagenesis from deep burial and heating,
 253 chemical changes should be minimal.

254 3.3. AMS and slumping

255 Cronin et al. (2001) investigated a section of lime-
 256 stone in Italy to define the paleomagnetic field in the
 257 Cretaceous Normal Supercron. The paleomagnetic data
 258 displayed several intervals in which the direction deviated
 259 significantly from the expected normal direction. Such
 260 data are often interpreted as excursions of the geomag-

netic field. In order to rule out slumping as a possible
 261 cause, they used AMS fabrics to characterize the
 262 “ordinary” and “deviant” intervals. The deviant intervals
 263 were triaxial, while the ordinary intervals were oblate.
 264 These results strongly suggest that the deviant directions
 265 were the result of crypto-slumping, which is soft
 266 sedimentary slumping sub-parallel to bedding that leaves
 267 little to no visible record in the outcrop.
 268

As suggested by Rosenbaum et al. (2000) and Cronin
 269 et al. (2001), it appears that even minor amounts of soft
 270 sediment deformation can have a profound effect on the
 271 paleomagnetic record. However, such deformation can be
 272 extremely difficult to detect based on visual observations
 273 alone, hence the term crypto-slump (Schwehr and Tauxe,
 274 2003).
 275

Schwehr and Tauxe (2003) pursued the idea that soft
 276 sediment deformation can be detected through the use of
 277 AMS by investigating both crypto-slumped sediments
 278

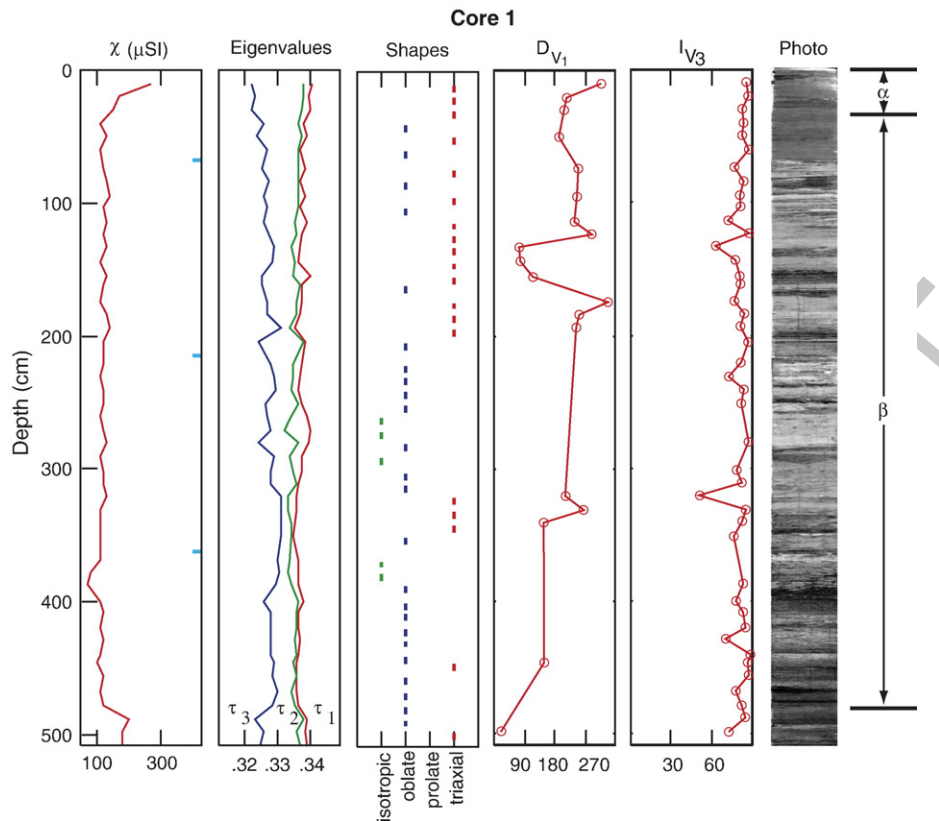


Fig. 7. Piston core 1 is located on the downslope limb of the wave structure. Note that the upper 200 cm of the core appears triaxial, whereas beneath this, the sample fabrics are predominantly oblate. The eigenvalues suggest a systemic decrease in the overall anisotropy down core. The density of V_1 and V_3 measurements compared to the number of samples in the shapes column appears low because many samples failed to pass the 95% F -test (Hext, 1963). The ticks on the right side of the χ_{lr} graph mark the boundaries where the core was cut into sections.

279 from a marine environment, along with the sediments
 280 from within and above the slump to confirm observa-
 281 tions of Cronin et al. (2001). They found a crypto-slump
 282 in a shale that can be traced laterally to a slumping event
 283 observed in the outcrop. Without the excellent exposure
 284 and lateral continuity along the outcrop, its slumped
 285 nature would not be easily detected. Schwehr and Tauxe
 286 (2003) then developed a test for post-depositional de-
 287 formation based on the AMS characteristics of slumped
 288 versus undeformed sediments.

289 In essence, the test assesses whether the V_3 directions
 290 are vertical and distinct from V_1 and V_2 , and whether the
 291 fabric is oblate (as expected for undisturbed sediment), or
 292 triaxial or prolate (as expected for disturbed fabrics). They
 293 used a statistical bootstrap approach to perform this test
 294 (see Constable and Tauxe, 1990; Tauxe, 1998 for more
 295 details).

296 The example from Schwehr and Tauxe (2003) shows
 297 that AMS is able to distinguish between sedimentary
 298 structures and deformation in situations where field
 299 observations are ambiguous. However, the AMS boot-

strapping technique developed by Cronin et al. (2001) 300
 and Schwehr and Tauxe (2003) may not be easily 301
 applicable to cores such as those collected in the Eel 302
 River Basin because of different compaction and de- 303
 formation states. Bootstrapping conducted by Cronin et al. 304
 (2001) and Schwehr and Tauxe (2003) grouped samples 305
 into stratigraphic layers; however, such sampling is not 306
 currently possible with today's coring technology. For 307
 each stratigraphic layer, there may be different magnetic 308
 grain distributions and concentrations in addition to the 309
 possibility of different flow regimes and directions. We 310
 employ bootstrap statistics on sediment zones in this 311
 study, but the results should be used with caution. 312

3.4. AMS applied to the Humboldt Slide 313

The two alternative hypotheses for the formation of 314
 the Humboldt Slide deposit (slope failure and sediment 315
 waves) predict very different fabrics that can be mea- 316
 sured using AMS. The deformational hypothesis of 317
 Gardner et al. (1999) predicts a triaxial fabric with the 318

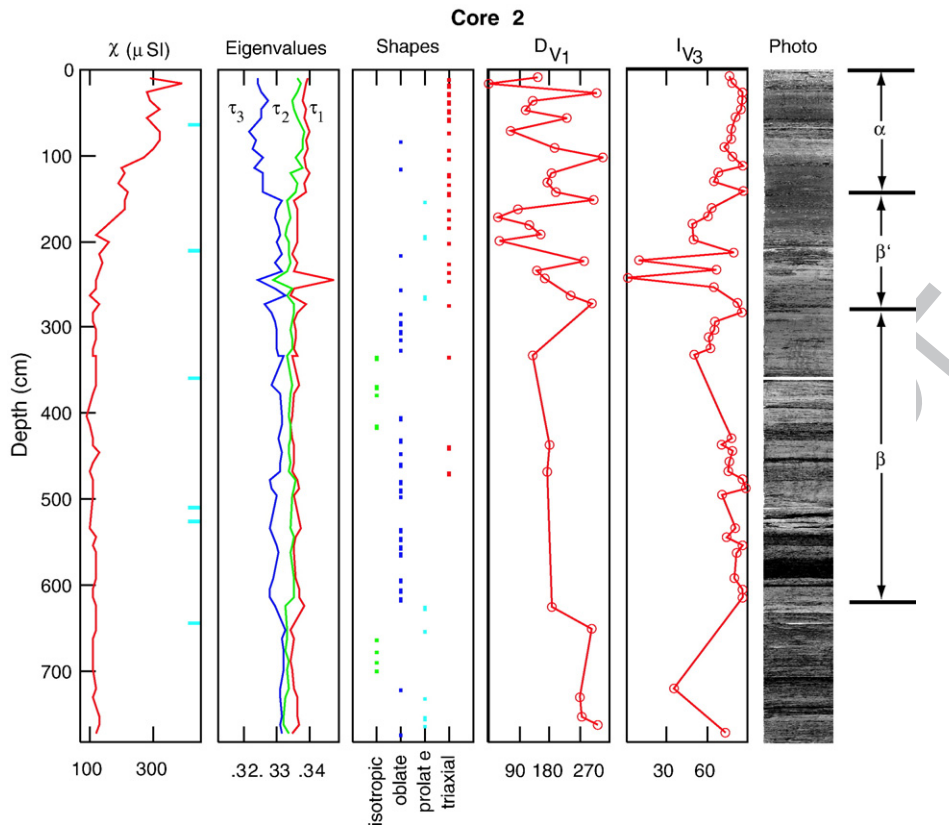


Fig. 8. At 100 cm core depth in piston core 2, there is shift in both χ_{if} and the eigenvalues that culminates at approximately 190 cm. This shift suggests two different sediment sources. Underlying this transition is a region that appears to be deformed (or have been deposited under high flow conditions) from 160 to 280 cm. Pervasive deformation throughout the core is not observed.

319 maximum axes of susceptibility (the V_1 eigenvectors)
 320 being either poorly grouped, perpendicular to the most
 321 compressive stress (see Fig. 3c), or approximately north-
 322 south. The density current hypothesis of Lee et al. (2002)
 323 predicts oblate fabrics with the minimum axis of sus-
 324 ceptibility (projected into the lower hemisphere) deflec-
 325 ted in the direction of paleocurrent flow (see Fig. 3b), or
 326 approximately westward. The center region of the core
 327 should display oblate AMS fabric if the features are
 328 depositional, whereas broad deformation will show
 329 dominantly triaxial fabric throughout.

330 3.5. Seismic data

331 Seismic lines covering the top half of the Humboldt
 332 Slide were acquired during August 1999 as part of the
 333 ONR STRATAFORM project (cruise TTN-096). The
 334 CHIRP seismic system (e.g. Schock et al., 1994; Quinn
 335 et al., 1998; Gutowski et al., 2002) is a modified
 336 EdgeTech XStar system with an ADSL link from the
 337 fish to the topside computers. The data were collected
 338 with a 50 ms sweep from 1 to 6 kHz. The XStar SEG-Y

records were processed with seismic-py and SIOSEIS 339
 (Henkart, 2006), and were plotted with pltseg. Fig. 4 340
 shows the section of the cruise data relevant to this study. 341

The Huntec data presented in Fig. 5 were collected 342
 during August 1995 on cruise W-2-95-NC. The data were 343
 processed with a combination of Sonarweb and seismic- 344
 py. A hydrophone (channel 2) is mounted on a tail behind 345
 the fish, which experiences a large amount of motion, so 346
 we processed only channel 1 (Galway, 2000). Huntec data 347
 from cruises W-2-95-NC and W-1-96-NC have been 348
 presented in Gardner et al. (1999) and Lee et al. (2002). 349

350 3.6. Coring

In November 2001, large-diameter piston cores were 351
 acquired using the Oregon State University Coring 352
 Facility on board the *R/V Thompson*. The core sites 353
 were selected based on CHIRP seismic data (Fig. 4) and 354
 on EM-1000 swath bathymetry (Fig. 2). P-code 355
 differential GPS was used to locate the core sites and 356
 yielded 10 m, or better, accuracy of the core location. 357
 Core locations and lengths are summarized in Table 1. 358

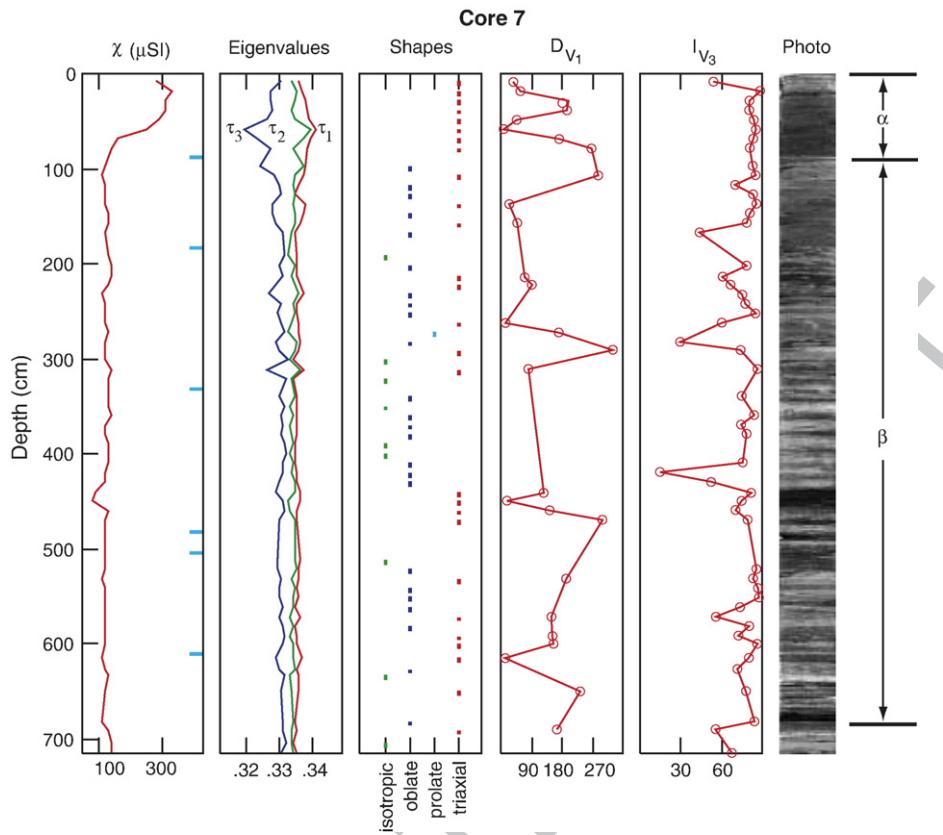


Fig. 9. Piston core 7. This core has the same shift in χ_{IR} observed in the other piston cores. There is no discernible trend in the D_{V1} . The I_{V3} shows a section with non-vertical vectors, but this is a small region and many of the samples are isotropic.

359 The lengths of the piston cores range from 5.9 to 7.8 m.
 360 The piston cores have an inner diameter of 10.2 cm
 361 which minimizes deformation associated with coring
 362 allowing undisturbed samples for AMS analysis to be
 363 acquired away from the liner effects.

364 Core 5 (Figs. 2 and 6), collected north of the Humboldt
 365 Slide, serves as a control because it is located in an area
 366 with minimal deformation based on the seismic and
 367 bathymetric data. Core 5 was collected at a depth similar
 368 to that of cores 1, 2, and 7 and is located in a portion of the
 369 slope characterized by gullies (referred to as rills) described by
 370 Spinelli and Field (2001). We predicted that the
 371 AMS for the control core would show a normal
 372 sedimentary fabric, perhaps with a signature of current
 373 flow down or across slope (i.e., gravity sheet flows or
 374 slope-parallel contourites).

375 Cores 1, 2, and 7 were acquired in the primary study
 376 site within the Humboldt Slide (Figs. 4 and 7–9). These
 377 cores sampled across the crest of one sedimentary structure
 378 located in the center of the Humboldt Slide at a water
 379 depth of 460 m. This feature has a wavelength of about
 380 150 m and an amplitude of approximately 6 m. Given fish
 381 layback uncertainty (as marked in Fig. 4), it is not possible

to determine exactly where on these structures each core
 was acquired; however, it is clear that the three cores have
 sampled both the upslope and downslope components of
 the slide on feature c. Note that the estimated core
 penetration is shown on Fig. 4.

3.7. Paleomagnetism

From the cores, we collected 8 cm³ paleomagnetic
 sample cubes with a typical sampling interval of 10 cm.
 The down core AMS measurements provide the key
 data for interpreting the Humboldt Slide as either a
 retrogressive failure or a downslope current-controlled
 deposit (i.e., sediment waves) infilling a slide scar.
 Magnetic measurements were performed at the Scripps
 Paleomagnetic Laboratory. NRM measurements were
 conducted on 3-axis CTF and 2-G cryogenic magnet-
 ometers (designated Bubba and flo respectively),
 located in a magnetically shielded room. Alternating
 field (AF) demagnetizations were accomplished using
 an SI-4. After best fit directions for each sample were
 found, the Fisher statistics (Fisher, 1953) were applied to
 each core section to get a best fit declination (D^- ,

Table 2

t.2.1	Core	Section	\bar{D}	\bar{I}	N	R	κ	α_{95}	Depth (cm)
t.2.1	1	1	217.2	67.5	6	5.3555	7	25.7	69
t.2.2	1	2	335.6	56.3	12	11.4192	18	10.2	216
t.2.3	1	3	319.3	49.5	12	10.8026	9	15.1	363
t.2.4	1	4	338.6	55.4	12	11.4111	18	10.3	508
t.2.5	2	1	85.0	58.7	4	3.9492	59	12.1	62
t.2.6	2	2	322.7	70.8	13	12.5929	29	7.8	209
t.2.7	2	3	279.3	62.0	11	10.4484	18	11.0	358
t.2.8	2	4	251.1	64.3	9	8.8349	48	7.5	507
t.2.9	2	5			0				525
t.2.10	2	6	293.5	68.0	5	4.8824	34	13.3	642
t.2.11	2	7	124.8	49.2	7	6.8468	39	9.8	783
t.2.12	5	1	132.1	36.8	13	12.8963	115	3.9	57
t.2.13	5	2	208.2	49.9	19	16.8045	8	12.5	207
t.2.14	5	3	225.9	49.9	3	2.9145	23	26.1	356
t.2.15	5	4	220.9	68.8	3	2.9699	66	15.2	505
t.2.16	5	5	254.9	66.8	7	4.7290	02	46.4	624
t.2.17	7	1	17.6	58.1	5	4.8088	20	17.1	87
t.2.18	7	2	39.7	63.5	7	6.7688	25	12.1	182
t.2.19	7	3	38.2	71.3	13	12.0803	13	11.9	330
t.2.20	7	4	67.8	58.5	3	11.5771	8	15.2	481

403 Table 2). \bar{D} was then applied to each core section such
 404 that the AMS eigenvectors are geographically oriented.
 405 AMS was measured on a Kappabridge KLY-2 using the
 406 same approach as is outlined in Schwehr and Tauxe
 407 (2003). ARM acquisition was accomplished with a SI-4
 408 using a 100 mT alternating field and a 40 μ T bias field.
 409 IRM's were imparted with an ASC impulse magnetizer
 410 with a field of 1 T.

411 A best fit tensor is derived from the 15 measurements
 412 made on the KLY-2 Kappabridge as a part of the AMS

413 acquisition. A bulk susceptibility (χ_{lf}) is calculated, and
 414 the eigenvalues presented are normalized to sum to 1. To
 415 determine the fabric shape, we use the F statistics of Hext
 416 (1963) (see also Tauxe, 1998). The F test checks for
 417 overall significance of anisotropy. If F_{ij} is below the 95%
 418 threshold for significance, the eigenvalues τ_i and τ_j are
 419 considered indistinguishable. Isotropic samples fail the
 420 F_{12} and F_{23} tests, therefore, all three eigenvalues are
 421 indistinguishable (Fig. 6: Shapes 1st sub-column —
 422 colored green). If the sample is anisotropic, then the F_{12}
 423 test checks for significance of the maximum and interme-
 424 diate eigenvalues and F_{23} for the intermediate and mini-
 425 mum eigenvalues. Oblate samples (2nd sub-column —
 426 colored blue) have τ_2 and τ_3 that are significantly
 427 different, whereas prolate samples (3rd sub-column —
 428 colored cyan) have τ_1 and τ_3 being significantly different.
 429 If the sample passes both F_{12} and F_{23} , then all three
 430 eigenvalues are distinct and the sample is termed triaxial
 431 (4th sub-column — colored red).

432 The V_1 declination (D_{V1}) shows the direction of the
 433 eigenvector associated with the maximum eigenvalue.
 434 This direction is only meaningful if the τ_1 eigenvalue is
 435 statistically distinguishable from τ_2 . Therefore, the V_1
 436 directions marked as prolate (cyan) and triaxial (red) in
 437 the Shapes column are significant. V_1 tends to be
 438 associated with the long axis of the magnetic grains. The
 439 V_3 inclination is meaningful when the fabric shape is
 440 either oblate or triaxial (τ_3 distinct from τ_2). The
 441 inclination of V_3 (I_{V3}) is often used as a proxy for
 442 detection of bed rotation (e.g. Rosenbaum et al., 2000;
 443 Kanamatsu et al., 2001; Housen and Kanamatsu, 2003).

Table 3

t.3.1	Core	Zone	V	\bar{D}	\bar{I}	η	D_η	I_η	ζ	D_ζ	I_ζ
t.3.2	1p	α	V_1	191.3	1.7	4.4	78.0	85.6	90.0	281.5	4.0
t.3.3	2p	α	V_1	169.1	5.1	9.0	309.9	83.5	90.0	78.7	4.1
t.3.4	5p	α	V_1	296.0	2.7	5.9	179.3	84.0	90.0	26.3	5.4
t.3.5	7p	α	V_1	213.4	1.9	10.3	355.8	87.7	77.5	123.3	1.4
t.3.6	1p	α	V_3	81.9	84.8	3.3	172.2	0.0	4.8	262.2	5.2
t.3.7	2p	α	V_3	306.1	83.1	6.3	86.6	5.4	7.5	177.0	4.4
t.3.8	5p	α	V_3	180.0	83.9	5.0	304.9	3.5	6.0	35.2	5.0
t.3.9	7p	α	V_3	18.5	88.1	9.2	198.1	1.9	10.8	288.1	0.0
t.3.10	2p	β'	V_1	154.8	24.4	40.0	316.6	64.5	90.0	61.6	7.0
t.3.11	5p	β'	V_1	52.3	3.6	23.3	302.6	79.3	90.0	142.9	10.0
t.3.12	2p	β'	V_3	325.1	65.3	40.7	155.3	24.4	90.0	63.5	3.9
t.3.13	5p	β'	V_3	302.5	79.4	16.5	89.4	8.9	21.0	180.3	5.7
t.3.14	1p	β	V_1	271.0	2.5	5.6	70.1	87.3	90.0	181.0	1.0
t.3.15	2p	β	V_1	154.3	11.4	9.3	353.5	78.0	90.0	245.1	3.8
t.3.16	5p	β	V_1	25.2	1.4	5.4	270.4	86.7	90.0	115.3	3.0
t.3.17	7p	β	V_1	161.9	0.0	7.6	252.0	83.9	74.6	71.9	6.1
t.3.18	1p	β	V_3	71.3	87.4	4.7	222.5	2.3	5.4	312.6	1.3
t.3.19	2p	β	V_3	347.7	78.3	8.5	171.8	11.7	9.0	81.6	0.8
t.3.20	5p	β	V_3	266.0	87.2	4.2	72.5	2.8	4.8	162.5	0.7
t.3.21	7p	β	V_3	252.0	84.6	6.8	343.2	0.1	8.3	73.3	5.4

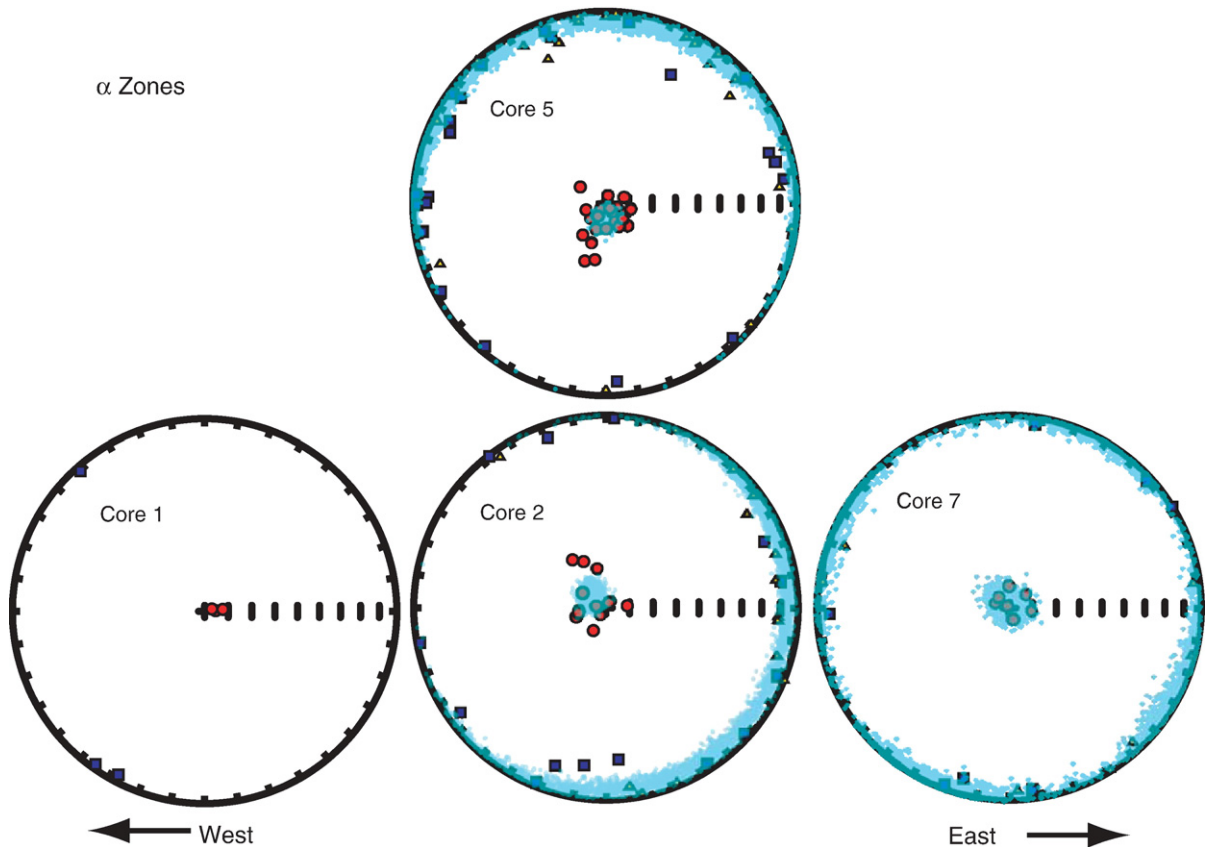


Fig. 10. α zones occur at the top of each of the piston cores. This zone is characterized by high χ_{1f} , anisotropy, ARM, and IRM. The individual shape fabrics are predominately triaxial. Bootstrap eigenvectors have a tight cluster near vertical. Blue squares are V_1 ; yellow triangles are V_2 ; and red circles are V_3 . The cyan dots are the bootstrap eigenvectors; V_1 – V_3 eigenvectors are not distinguished. (For interpretation of the references to colour in this figure legend, the reader is referred to the web version of this article.)

444 After magnetic measurements were made, the
 445 samples were wet sieved to remove the clay to medium
 446 silt fraction using a 47 μm screen. Finally, a range of
 447 grain size separates were sieved to determine silt, sand,
 448 and organic debris fractions; the organic debris included
 449 branches, twigs, seeds, etc.

450 4. Results

451 Cores 1, 2, and 7 were collocated with CHIRP seismic
 452 data to constrain the geometry and stratigraphy of the
 453 three prominent highs being studied (marked a–c in
 454 Fig. 4). These three cores were collected across high c.
 455 The seismic reflection data were used to determine where
 456 to sample the features because in certain areas the
 457 deformed features are mantled by a pelagic drape. The
 458 thickness of the drape varies systematically from the top
 459 of the slide complex to the base (Fig. 5). At the top of the
 460 slide structure, there is little to no detectable pelagic drape
 461 overlying the deformed features at the locations of cores 1,
 462 2, and 7 as observed in the CHIRP and Hunttec seismic

lines (Figs. 4 and 5a). Examination of our core locations
 (Fig. 4) and co-registered seismic data reveal that all three
 cores penetrated through any pelagic drape into the
 underlying sedimentary features.

The CHIRP system imaged faint seaward dipping
 reflectors with high-amplitude landward dipping reflectors.
 There is a marked asymmetry with the landward dipping
 sequences being much thicker than the seaward dipping
 units. In fact, across some features only the landward
 dipping sequences are observed with individual horizons
 cropping out at the sea floor on the seaward slope

(Fig. 4a).
 The first test to determine if post-depositional
 deformation occurred is to examine the NRM directions
 for evidence of rotation. The seaward and landward
 limbs of these features (Fig. 4a–c) exhibit a range of
 dips from 2.1° to 4.1° (Fig. 4: inset table). Cores 1, 2 and
 7 penetrate structure c which has a seafloor landward
 slope of 2.2° and a seaward slope of 4.1°. If there is E–
 W compression or rotation with a northerly fold axis,
 there should be a shallowing of approximately 0.5° in

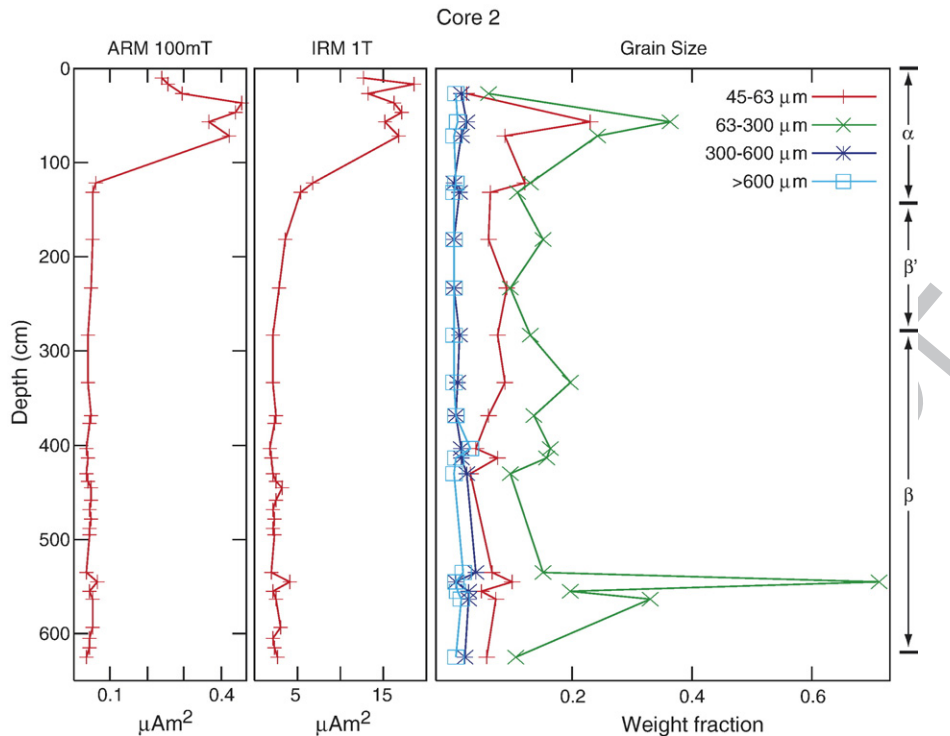


Fig. 11. Anhyseretic remanent magnetization (ARM) and isothermal remanent magnetization (IRM) show an abrupt decrease from α to β' . There is a distinct difference in the ARM and IRM in the first meter of the core. There is a much higher concentration of magnetic grains and a different grain population. The 300 and 600 μm sieves were selected to sort out the vascular planet material, where the $>600 \mu\text{m}$ material is predominantly twigs and branches. The 63–300 μm range captures the sand fraction, while the 45–63 μm range captures the coarse silt fraction.

484 the NRM inclination compared to the expected
 485 geocentric axial dipole (GAD) inclination of 60.0° .
 486 Given that the α_{95} confidence values range from 8 to
 487 26° (Table 2: cores 1, 2, and 7), such small rotations are
 488 below the resolution of this approach, and therefore, we
 489 must rely on the AMS technique for detecting post-
 490 depositional deformation.

491 The AMS results are shown in Figs. 6–9. Core 5
 492 (Fig. 6) was collected as a control for this study and as
 493 such, it is located outside of the Humboldt Slide. Cores
 494 1, 2, and 7 were acquired within the slide feature to
 495 assess whether the sediment carapace has experienced
 496 rotation and deformation. Based on the observation of
 497 the AMS fabric observed in the cores, four distinct
 498 zones termed α , β , β' , and γ were identified. Core 5
 499 is used as the “type section” because it exhibits all four
 500 zones. Here we will describe the characteristics that
 501 define the four zones.

502 4.1. α — alpha

503 The first zone, α , is characterized by high suscepti-
 504 bility and high anisotropy observed in the AMS data.

Individual samples exhibit a predominantly triaxial
 AMS fabric type with near-vertical orientation of the
 minor eigenvector (see Figs. 6–9: I_{V3}). The Hext (Hext,
 1963) average inclination of V_3 for a group of samples is
 recorded in Table 3 as \bar{I} . The V_1 eigenvectors, as
 observed in the equal area projection (Fig. 10), have no
 preferred orientation (Figs. 6–9: D_{V1}). The confidence
 ellipses and best fits derived by bootstrap statistics for
 the different zones are reported in Table 3. The α zone is
 also characterized by large ARM, IRM and χ_{lf} (we plot
 only χ_{lf} in Figs. 6–9). An increase in the coarse silt
 fraction correlates with the boundary between α and β'
 in core 2 (Fig. 11: grain size). When plotting IRM versus
 χ_{lf} , the different zones can be delineated as shown in
 Fig. 12. α exhibits high and transitional χ_{lf} , ARM, and
 IRM, whereas low χ_{lf} , ARM, and IRM are characteristic
 of the other zones (Fig. 12).

522 4.2. β' — beta prime

523 The β' zone is observed in cores 2 and 5 and is
 524 characterized by rotation of the V_3 eigenvectors away
 525 from vertical determined for the individual sample

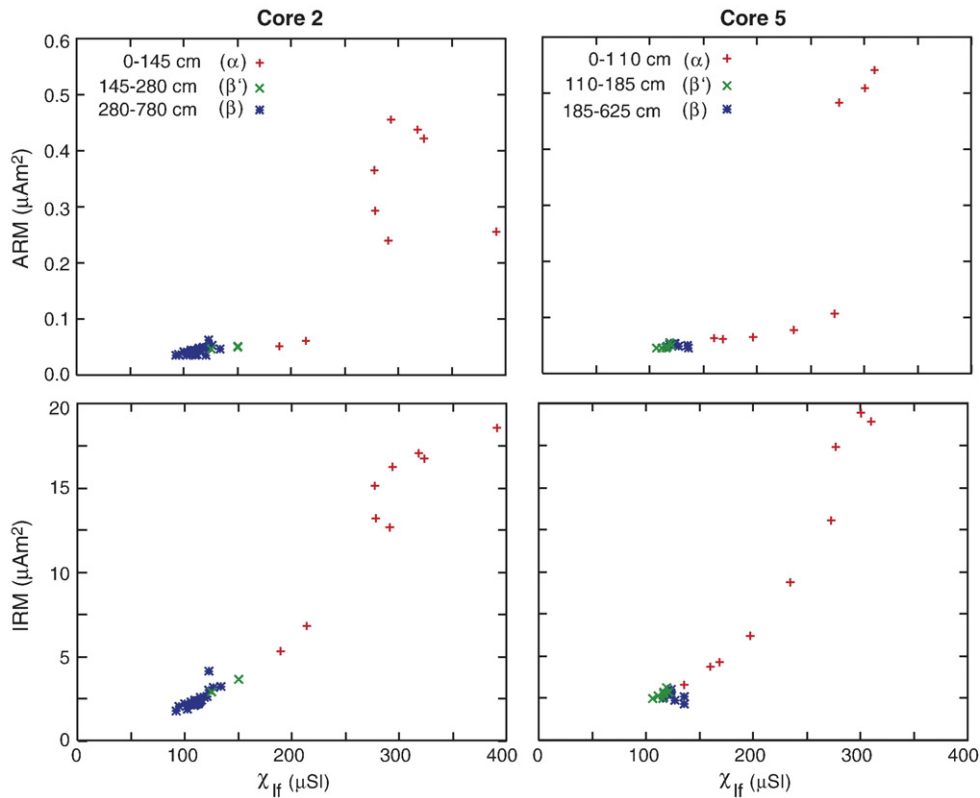


Fig. 12. Core 2 and 5 Banerjee plots. Banerjee et al. (1981) showed that a χ_{lf} versus ARM plot can show grain size for magnetites based on the slope of a line that passes through the origin. In this figure, cores 2 and 5 show three distinct groups. The top of the core exhibits high χ_{lf} , ARM, and IRM with a transition zone in the middle down to the lower χ_{lf} , ARM, and IRM in the deeper section of the core. Comparing to Fig. 11, one can see that shifts in grain size do not necessarily lead to the same change in the magnetic grains.

526 measurements (Figs. 6 and 8: I_{V3}). The deflection of V_3
 527 away from the vertical is also observed in the equal area
 528 projections (Fig. 13). A marked decrease in total

anisotropy as evidenced by the eigenvalues is also 529
 characteristic of the β' zone. (Figs. 6 and 8). V_1 exhibits 530
 slightly more grouping in β' than in the overlying α zone, 531

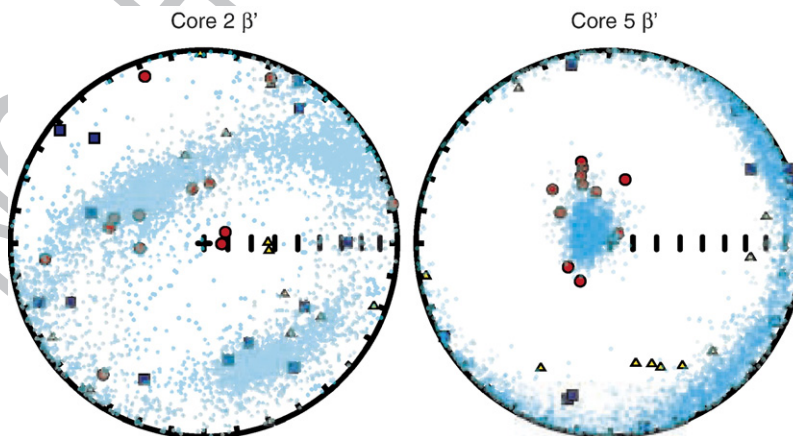


Fig. 13. β' zones occur between α and β and has intermediate values of total anisotropy and bulk susceptibility. The individual shape fabrics are predominately triaxial. Note that there are a number of prolate samples in these two β' zones (see Figs. 6 and 8). Unlike α and β , β' has V_3 vectors that are deflected from vertical.

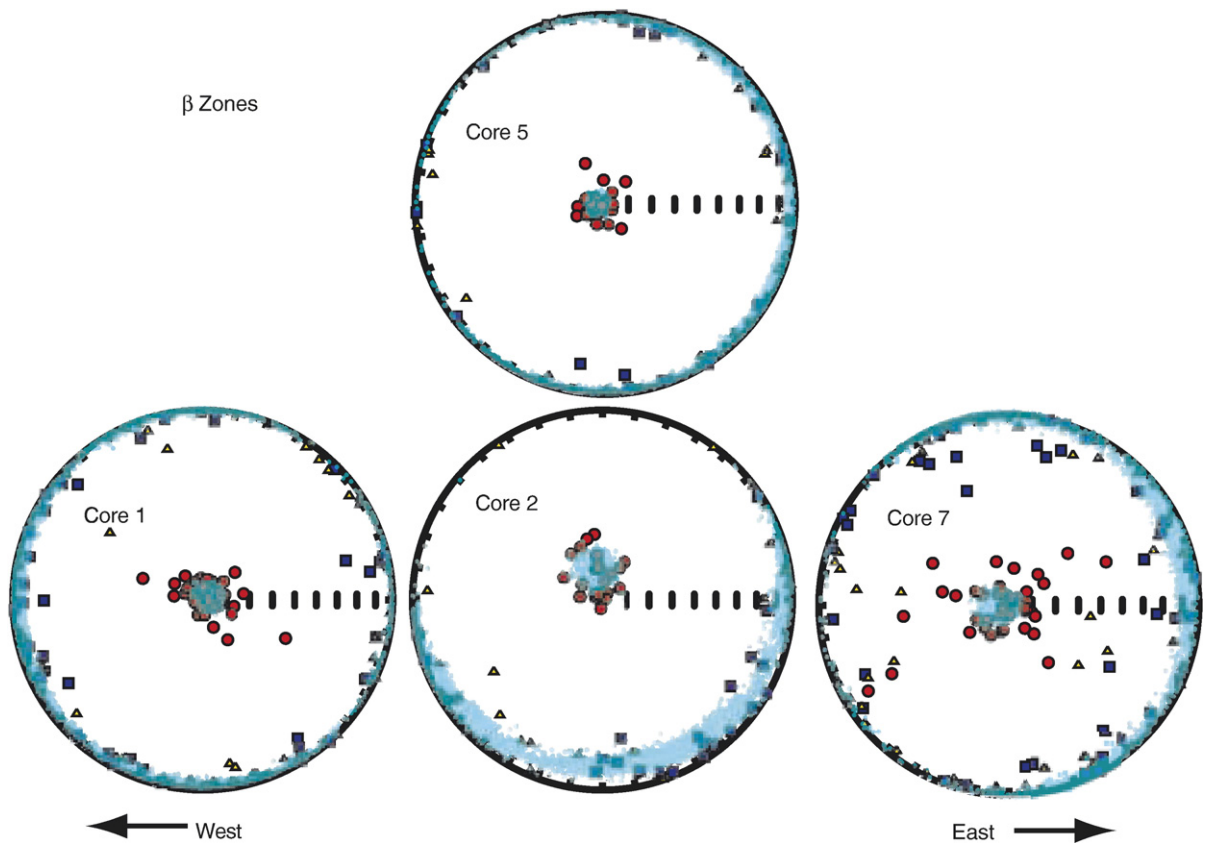


Fig. 14. β zones are characterized by lower anisotropy, ARM and IRM compared the α zones. Individual sample shape fabrics are mostly oblate with some isotropic and triaxial samples. Bootstrap eigenvalues have a tight cluster near vertical. For all except core 7, the V_3 are near vertical. Core 7 has a number of small zones with non-vertical V_3 that may record deposition in a moderate current because there is no preferred orientation for V_1 .

532 nevertheless a strong preferred orientation is not observed
 533 (Fig. 13). The AMS fabrics for individual samples are
 534 predominately triaxial for the β' zone.

535 4.3. β — beta

536 Underlying the β' zone in cores 2 and 5, there is a
 537 pronounced shift to more oblate fabric for individual
 538 samples in the β zone. However, the transition from β'
 539 to β is not well defined by either the eigenvalues or χ_{lf} .
 540 In cores 2 and 5, the β zone is defined by near-vertical
 541 V_3 orientation with tight clustering (Figs. 8 and 6: I_{V_3}).
 542 Note that in core 7, even though the eigenvalues by
 543 sample show some scatter, the bootstrap vectors show a
 544 tight cluster near vertical (Fig. 14).

545 In cores 1 and 7, β' is not observed and the α zone
 546 mantles β . When α directly overlies β , the zones are
 547 delineated by a marked shift in χ_{lf} (Figs. 7 and 9). In core
 548 7, a marked decrease in overall anisotropy appears to
 549 correlate with the boundary between α and β . In core 1,
 550 the decrease in overall anisotropy is more subdued for the

transition between α and β (Fig. 7) than in the other cores. 551
 In the β zone, V_1 for all cores shows weak grouping; 552
 however, there does not appear to be a preferred orienta- 553
 tion for β . As mentioned before, β is characterized by 554
 low χ_{lf} , ARM, and IRM (Figs. 11 and 12). 555

In all four cores, only small zones of bioturbation are 556
 observed. In general, the layering is clearly visible, and 557
 undisturbed as revealed by the core photos. The bound- 558
 aries between layers are sharp, and mottling and smear- 559
 ing of layer boundaries is not commonly observed. 560
 A large number of organic-rich layers are clearly visible 561
 in the cores with a maximum thickness of 30 cm (core 2 562
 from 568–589 cm for the vascular plant material deposit; 563
 Fig. 6). 564

The core photos show a reciprocal relationship for 565
 the β zone and the occurrence of dark, organic-rich 566
 layers depending on whether the cores were acquired 567
 within or outside the slide region. Cores 1, 2, and 7 show 568
 an increase in occurrence and thickness of dark organic- 569
 rich layers in the β zone compared to the α zone. The 570
 dark organic-rich layers are comprised mostly of 571

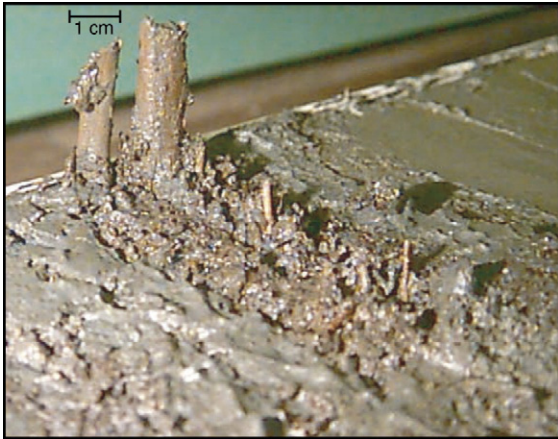


Fig. 15. Oblique photograph of core four inside the Humboldt Slide located at 124° 29.055' W, 40° 50.106' N in 419 m of water. The plant matter shown here (at 130 cm from the core top) illustrates frequent flood layers from the Eel River are deposited in the Humboldt Slide region.

572 vascular plant matter (Fig. 15). In core 5, the α , β' ,
 573 upper β zones are characterized by dark organic-rich
 574 layers, while the lower beta zone is largely devoid of
 575 such layers. In core 5, the thickest dark, organic-rich
 576 layers occur in the γ zone (Figs. 6 and 16).

577 4.4. γ — gamma

578 The γ zone is only observed in core 5, which was
 579 acquired to the north of the Humboldt Slide. γ is
 580 characterized by a marked deflection of V_3 from vertical
 581 in both the individual and group samples (Figs. 6 and 17).
 582 In core 5, the β zone above and below the γ zone is
 583 characterized by oblate fabric, with γ being predominate-
 584 ly triaxial. The γ zone is indistinguishable from β based
 585 on χ_{lf} eigenvalues, ARM and IRM. Within the γ zone,
 586 the sediments appear to show signs of post-depositional
 587 deformation as a dark, organic-rich horizon may have
 588 been folded (Fig. 16: inset).

589 5. Discussion

590 In order to fully understand a marine slump, it is
 591 helpful to review the features that are typically expected.
 592 Comparison with a small slide exhibiting minimal run out
 593 shows markedly different features than those observed in
 594 the Humboldt Slide. Fig. 18 is a CHIRP seismic image of
 595 the Gaviota Slide from the Santa Barbara Basin that
 596 exhibits features typical for many slides and provides
 597 valuable insights for the expected sedimentary structures
 598 and morphology (Schwehr et al., in press). For the

Gaviota slide, the failed material has not moved far
 downslope with minimal translation from the evacuation
 to accumulation zone. If the failure is retrogressive in
 origin, then after initiation, the failure propagates upslope
 from the point of initial failure and terminates at a head-
 wall scarp. Along the seaward extent of the slide complex,
 the toe often exhibits signs of compressional deformation
 (Fig. 18). The V_1 eigenvalues showed a preferred
 orientation as a result of downslope compression (Fig.
 18: inset). Between the upper headwall scarp and the toe,
 there is an evacuation zone, where the material has
 vacated, or a zone of thinned and extended material.

According to Gardner et al. (1999), the Humboldt
 Slide is thin skinned; however, little or no accommoda-
 tion zone for this slide is observed. This does not match
 the model for other slides where either a catastrophic
 failure mobilizes the sediment into a turbidity current, or
 sediment is removed from an evacuated zone to an
 accumulation zone downslope (Fig. 18).

The morphology of the Humboldt Slide suggests
 minimal translation down-slope because there is no
 downslope thickening or upslope thinning. Furthermore,
 the MCS data acquired across the region images
 individual layers that thicken and diverge toward the
 margin. The divergence of the horizons and the
 diminished dip up section may reflect long-term tectonic
 control in the region, suggesting fault-controlled accom-
 modation (e.g., Driscoll and Hogg, 1995). Onlap and
 thinning are observed across the Little Salmon Anticline.

Lee et al. (2002) presented numerous lines of
 evidence based on stratal geometry and morphology
 that the Humboldt Slide features are current-controlled
 bedforms. Nevertheless, based on the same internal
 geometry and morphology Gardner et al. (1999) argued
 that these features are the consequence of post-depo-
 sitional deformation. As previously mentioned, mor-
 phology is not unique and thus, the debate concerning
 the origin of these features continues. AMS measure-
 ments provide additional constraints on the origin of
 these features and are discussed below.

5.1. α — alpha

The high χ_{lf} , ARM and IRM characteristic of the α
 zone is different than the other underlying zones
 observed in the cores. Given that the high ARM and
 IRM values are only observed in the upper sections of
 the cores, Figs. 11 and 12 suggest that the base of α
 is either (1) a diagenetic front delineating the top of
 the sulphate reduction zone, where biomediation con-
 sumes a fraction of the ferro magnetic grains; or (2) a
 mineralogical change reflecting a change in sediment

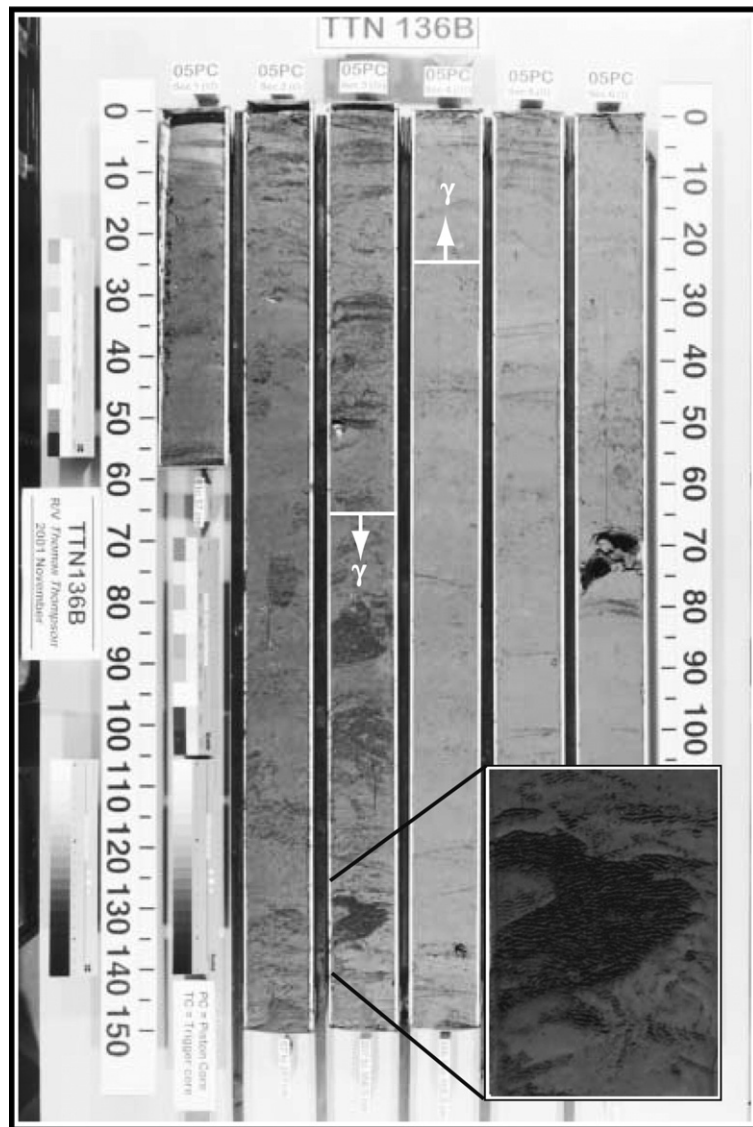


Fig. 16. Core 5 photograph. The inset shows an apparent folded layer within the deformed γ zone.

649 discharge from the Eel River system. Diagenetic
 650 signatures in rock magnetic parameters (e.g. χ_{lf} , ARM,
 651 IRM) have been reported by numerous authors from a
 652 wide range of environments around the world (e.g.
 653 Karlin, 1990b; Leslie et al., 1990b; Tarduno, 1994; Liu
 654 et al., 2004; Geiss et al., 2004; Kumar et al., 2005; Pan et
 655 al., 2005; Riedinger et al., 2005; Rowan and Roberts,
 656 2006). These transitions are typically attributed to a
 657 sulfate reduction in sediments that preferentially consume
 658 magnetites with large surface area to volume ratios (e.g.,
 659 smaller grain size). Karlin (1990b) concluded that
 660 magnetic mineral diagenesis is likely to occur in rapidly
 661 deposited, sulfidic sediments. The process may shutdown
 662 after the initial reactions, not because of the complete

removal of magnetite, but from the magnetites becoming
 covered in a protective coating of pyrite (Egli, 2004).

The ARM versus χ_{lf} bi-plots show that the α zone is
 separate from the other zones that have moderate or low
 ARM and IRM values (Fig. 12). King et al. (1983)
 reported that for a line passing through the origin and
 through a group of measurements on an ARM versus χ_{lf}
 plot (they use χ_{ARM} , which is a normalized form of
 ARM), the slope of the line is related to the size dis-
 tribution of the magnetites in the samples. Steeper
 slopes are indicative of finer grained magnetites, where-
 as shallower slopes are evidence for coarser grained
 magnetites. If this relationship holds for the sediments in
 this study, then the most recently deposited sediments

663
 664
 665
 666
 667
 668
 669
 670
 671
 672
 673
 674
 675
 676

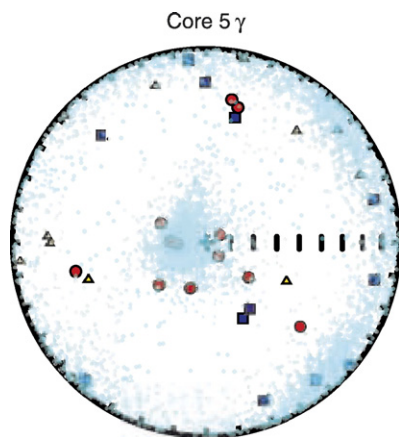


Fig. 17. The γ interval is only observed in Core 5. This zone is located between two β zones. γ has triaxial samples, low χ_{lf} , and V_3 vectors that deviate significantly from vertical.

677 (the tops of the cores, α zone) have a finer grained
 678 fraction of magnetites than the underlying zones. These
 679 magnetites are consumed in the reaction front and are no
 680 longer present in the deeper sediments. This hypothesis
 681 implies that the finer grained magnetite population is
 682 situated in such a fashion as to generate a triaxial fabric.
 683 Below the diagenetic front where the finer-grained
 684 magnetites have been consumed, an oblate anisotropy is
 685 observed for the individual samples (Figs. 6, 7, and 8). It
 686 is difficult to explain why the fine-grained magnetites
 687 have such strong anisotropy and thus it is not our
 688 preferred hypothesis. Unfortunately, dissolution of the
 689 finer grained fraction makes no prediction of the source
 690 of this easily reduced magnetite.

691 The second hypothesis is that α correlates with a shift in
 692 sediment provenance. There is a higher weight percent
 693 fraction of 63–300 μm grains in the α zone with respect to
 694 the underlying zones (Fig. 11). The Eel River area is
 695 undergoing a number of changes that could have caused
 696 such a shift. The shift may correlate with the 1955
 697 transition to an increase in frequency of large floods on the
 698 Eel River and the widening of the Eel River channel
 699 observed by Sloan et al. (2001) and Sommerfield et al.
 700 (2002). High flow conditions can cause sediments
 701 deposited to have triaxial fabrics (e.g. Kopf and Berhman,
 702 1997), which may explain the triaxial samples in α . If the
 703 density flows associated with these floods exhibit
 704 different flow directions through the Humboldt slide
 705 amphitheater, then they might produce the signature
 706 observed in Fig. 10 where the triaxial samples girdle the
 707 horizontal plane giving an overall group signature of
 708 oblate sediment fabric.

709 In rapidly depositing sediments, it is possible that the
 710 rate of deposition and sediment composition control the

location of a diagenetic front. Therefore, we can not rule
 out the possibility that the local shift in the Eel River
 sediment delivery system may play a role in governing
 the location of the transition from high to low χ_{lf} , ARM,
 and IRM.

The results for the α zone show conflicting model
 interpretations based on that presented in Fig. 3 and are
 difficult to interpret. The α zone bootstrap inclinations
 (Table 3: \bar{I}) range from 83.1° to 88.1°. This tight vertical
 V_3 implies quiet water deposition as illustrated in
 Figs. 3a. Cores 2 and 5 show the strongest evidence for
 flow directions of 306° and 180° respectively based on
 $V_3 \bar{D}$ (Table 3).

On the other hand, with the majority of samples being
 triaxial, one might be tempted to classify the sediments as
 deformed based on the triaxial histogram shown in
 Fig. 3c. It is important to distinguish the difference between
 sample level anisotropy (Figs. 6–9) and group level
 anisotropy (Fig. 3: bootstrapped eigenvalues). A group
 level bootstrap histogram tests for coherent deformation,
 whereas sample level anisotropy test for the statistical
 distinguishability of the eigenvectors for one specimen. A
 triaxial sample can imply a number of sediment histories
 including deformation or deposition under moderate flow
 conditions. Based on the observations, we interpret alpha
 to be indicative of deposition in moderate flow conditions.

5.2. β' — beta prime

The β' zone is only observed in cores 2 and 5 and is
 characterized by V_3 deviating from vertical. β' has
 relatively stable χ_{lf} , ARM, and IRM. The individual
 samples are predominantly triaxial, but there are several
 samples that are prolate. Nevertheless, the V_1 orientation
 shows no preferred direction in the bootstrap. We
 interpret this to be moderate to strong flow conditions
 and core 2 may be on the apex of the feature which may
 have exposed this location to slightly greater currents
 and/or erosion. Conversely in core 5, the V_3 does not
 exhibit as much deflection, which may be indicative of
 more moderate flow. Core 2 sampled high flow conditions
 that appear to be centered on 325° (Table 3), which
 would be consistent with predicted flow directions. The
 observation that cores 1 and 7 do not exhibit β' zones
 implies that the β' zone observed in core 2 is a local
 feature with little lateral extent.

5.3. β — beta

The marked shift to more oblate sample and group
 shape fabric defines the β zone, which implies quiet
 water deposition. This conclusion is a bit surprising

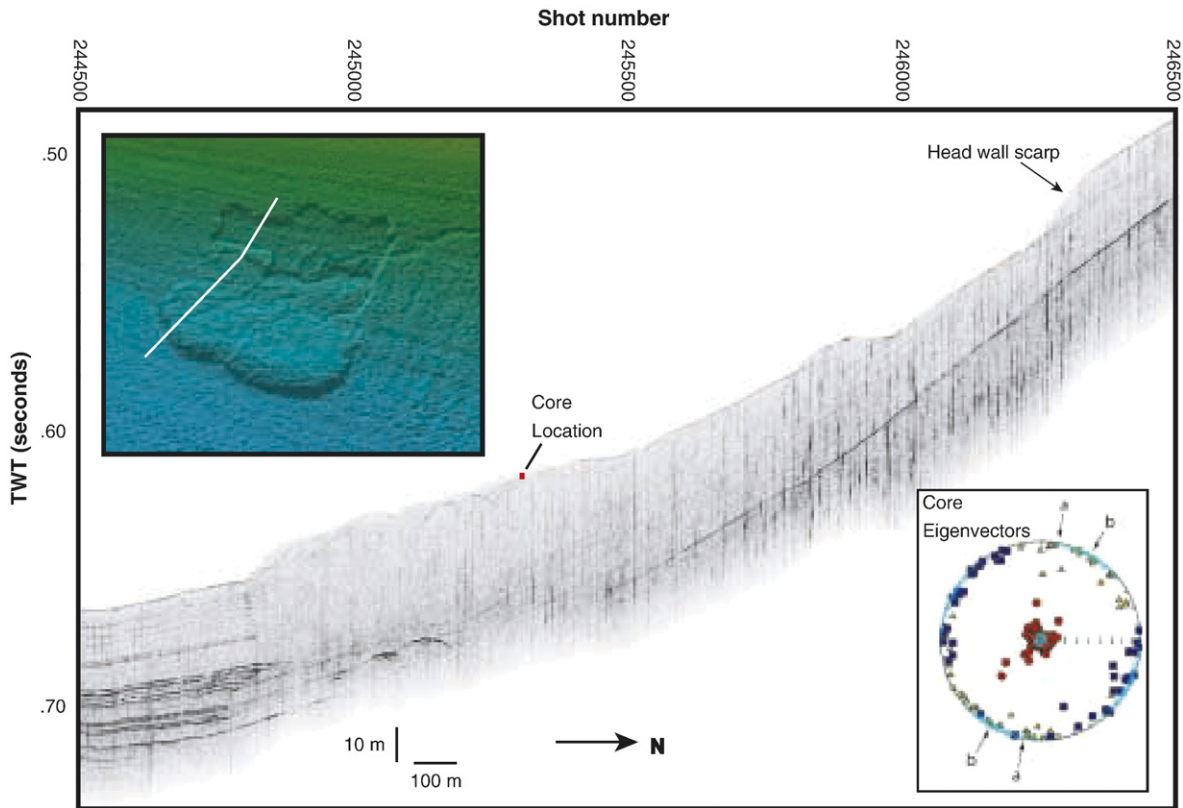


Fig. 18. A CHIRP seismic profile images the Gaviota Slide in the Santa Barbara Basin, southern California (Schwehr et al., in press). Note the clearly defined head scarp and thickening in the accumulation zone at the base of the slide. The inset shows the slide in EM300 from MBARI (Eichhubl et al., 2002). The expected direction of compression based on morphology is indicated by arrow (a). The direction of compression from the eigenvectors, shown by arrow (b), closely matches.

759 considering the size and frequency of large organic-rich
760 layers within the zone (e.g. Fig. 8: β and 15). This may
761 be caused by how flows attach to and detach from the
762 bottom as they travel over an undulating sea floor.

763 This is the zone where the best evidence should be
764 found for the deformation predicted by the slope failure
765 model (Gardner et al., 1999). The geometry observed in
766 CHIRP and Huntet seismic data (Figs. 4 and 5) predict
767 thickening of 2:1 or greater on the upslope limbs. This
768 amount of compression is expected to create fabric like
769 that illustrated in Fig. 3c. However, the eigenvectors
770 plotted on stereonet with bootstrap eigenvectors for β
771 most closely resemble Fig. 3a. Core 7 is the least like Fig.
772 3a, but the bootstrap eigenvectors are tightly clustered
773 near vertical. The scatter in the eigenvectors can be
774 traced to samples in four discrete regions located at
775 $\sim 167, 261\text{--}282, 420\text{--}430,$ and 572 cm. These layers
776 with V_3 deflected from the vertical might correspond to
777 periods of higher flow. Because the V_1 eigenvalues
778 shows no preferred orientation for β in Core 7, it does not
779 appear to be recording post-depositional deformation.

5.4. γ — gamma

780 γ stands out as the largest region of deflected V_3 . The
781 I_{V_3} has a saw-toothed pattern indicating deformation
782 that may not be coherent. This observation is supported
783 by visual inspection of the core photograph, which
784 shows a folded organic-rich layer (Fig. 16). Given the
785 degree of deformation in γ , it is difficult to assess the
786 direction of compression for this slump. The bootstrap
787 \bar{D} for V_1 is 330° , but this value has an associated ζ of
788 90° , meaning that \bar{D} for V_1 is not significant. However,
789 the lack of preferred orientation of V_1 in the bootstrap
790 test is consistent with highly deformed and folded
791 sediment (e.g., recumbent folding). Such a deformation
792 pattern exhibits fabrics in the AMS that are similar to
793 deposition under moderate to high flow conditions. Note
794 that γ looks very different from the eigenvectors from
795 the Gaviota Slide shown in Fig. 18 and much more like
796 β' in core 2. Nevertheless, visual examination of the core
797 indicates that the fabric is associated with folding and
798 deformation (Fig. 16).
799

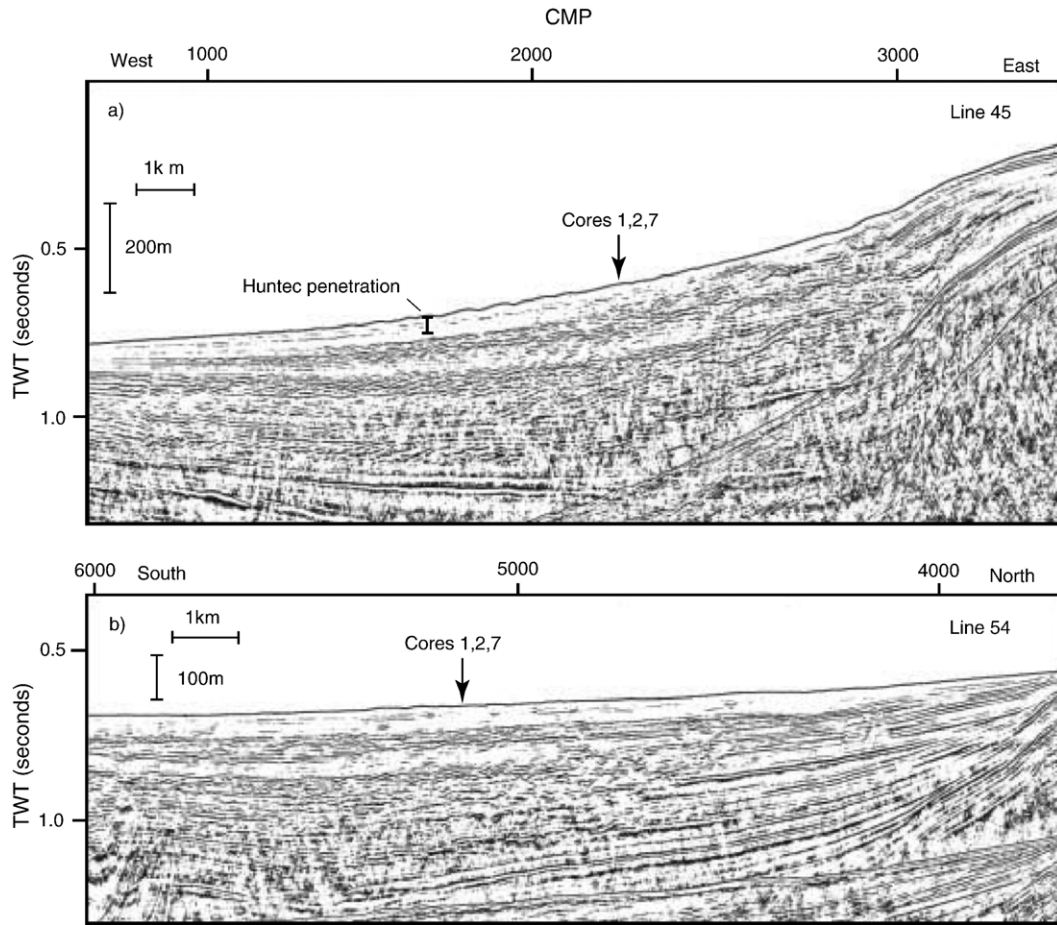


Fig. 19. Cruise W9605B multi-channel seismic lines. Line 45 is a dip line imaging the internal structure of the Humboldt Slide. Line 54 is a strike line across the region that includes the Little Salmon Anticline on the northern side. The location of cores 1, 2, and 7 is marked with an arrow. Line 45 runs from CMP 770 to 3323 that spans 16.0 km. Line 54 is 14.6 km long, from CMP 3698 to 6017.

800 5.5. The Humboldt Slide as a sediment wave field

801 We interpret the magnetic and sedimentological data
 802 presented here to indicate that there is little to no post-
 803 depositional deformation in the Humboldt Slide region.
 804 On the basis of the AMS data, we have identified four
 805 types of sediment. There is evidence for moderate to
 806 strong flow events and small crypto-slump events (usually
 807 occurring as a number of events in a restricted region).
 808 These crypto-slump events may represent periods of rapid
 809 sea level change, high sediment accumulation rates and
 810 loading, or increased seismic activity, but currently there
 811 is insufficient evidence to test these hypotheses.

812 The rill area to the north of the Humboldt Slide shows
 813 greater evidence for deformation in comparison to the
 814 material in the Humboldt Slide amphitheater. The over-
 815 lying several meter sediment package may be creeping
 816 over the underlying sediments.

We observe no evacuation zone or downslope thickening toward the toe of the slide. The units observed in the MCS data (Fig. 19a; described in Burger et al., 2003) thin seaward down the slide. Individual layers exhibit divergence and thickening towards the margin that may reflect long-term tectonic control in the region (Fig. 19b). The stratal geometry imaged in the MCS data is not consistent with the geometry predicted by the retrogressive failure model.

There is a geometric problem with this feature being interpreted as a slide deposit as it exhibits no thinning in the evacuation zone and no thickening in the accumulation zone. This implies that all deformation is accommodated by in-situ rotation and thickening of beds, with little to no translation. We are unable to identify any signature of such processes beyond occasional thin layers that appear to be deposited in moderate to high flow conditions. The orientation of the

835 V_1 eigenvalues is not suggestive of post-depositional
836 deformation as observed in the Gaviota Slide region
837 (Fig. 18).

838 These observations support the hypothesis that these
839 features are sediment waves with preferential deposition
840 on the upslope limbs. The sediment waves are com-
841 posed of both hemipelagic deposits and event beds.
842 Near the base of core 1, 2, and 7, (Figs. 7–9) there is an
843 increase in frequency and thickness of layered units
844 down core. Wood and plant material occurs more fre-
845 quently down core with some layers being >20 cm
846 thick. This suggests a change in the style and/or type of
847 flood deposits as compared to the present.

848 6. Conclusions

849 The main results of our rock magnetic and seismic
850 reflection study are summarized as follows:

- 851 (1) The upper ~ 8 m of the Humboldt Slide sediments
852 are not undergoing post-depositional deformation
853 and folding.
- 854 (2) The upper section sampled in this study appears to
855 be the result of primary deposition, and thus, we
856 interpret the features to be downslope current-
857 controlled bedforms.
- 858 (3) Based on MCS data, the thickness and dip of the
859 subsurface sequences are not consistent with the
860 features being a slide deposit. The sediment
861 structures within the Humboldt Slide appear to
862 be sediment waves that may mantle an older slide.
- 863 (4) We identified a ~ 1 m thick slump layer located to
864 the north of the Little Salmon Anticline in the
865 region with extensive rills.
- 866 (5) The change in how much and what fraction of
867 material is delivered to the Humboldt Slide area
868 (versus that north of the Little Salmon Anticline
869 and down the Eel Canyon to the south) may have
870 undergone a recent shift caused by the increasing
871 frequency of combined large storm and flood
872 events from 1955 to the present. This possibility
873 requires further research.

874
875 Magnetic measurements allow us to test between the
876 alternative hypotheses of slope failure, and sediment
877 waves for the origin of the Humboldt Slide. Specifically,
878 we are able to discern whether the morphology and
879 internal geometry results from soft sediment deforma-
880 tion and retrogressive slumping, or downslope current-
881 controlled deposition. The former predicts a triaxial
882 AMS fabric with essentially north-south oriented
883 maximum axes (Fig. 3c); the latter predicts an oblate

884 fabric with a possible westward deflection of the mini-
885 mum axes (Fig. 3a,b).

886 The morphology and internal architecture of the
887 Humboldt Slide are not unique; there are numerous
888 examples along other continental margins with similar
889 morphology and ongoing debates regarding their origin
890 (see examples in Lee et al., 2002). Magnetic methods for
891 the detection of post-depositional deformation provides
892 a new approach to determine the origin of such features
893 on other continental margins.

894 Acknowledgments

895 We would like to thank NSF (grant OCE-04-25919),
896 ONR (grant N00014-03-1-0272), and CalIT² for fund-
897 ing this research. Additionally we appreciate the support
898 of the crew of the *R/V Thompson*, the OSU Coring
899 Group, the Nittrouer lab and the SIO Geologic Col-
900 lections. J. Borgeld and his students from Humboldt
901 State University helping out with the cruise. H. J. Lee
902 and J. Gardner provided numerous comments and dis-
903 cussions. J. Gardner provided support in processing the
904 Huntex seismic data. The MCS images (IDs: 4213 and
905 4226) were acquired from <http://www.ig.utexas.edu/sdc/cruise.php?cruiseIn=w9605b>, courtesy of C. Fulthorpe
906 and G. Mountain.
907

908 References

- Alexander, C.R., Simoneau, A.M., 1999. Spacial variability in sedi-
909 mentary processes on the eel continental slope. *Mar. Geol.* 154 (1–4),
910 243–254.
911
Banerjee, S.K., King, J., Marvin, J., 1981. A rapid method for magnetic
912 granulometry with applications to environmental studies. *Geophys.*
913 *Res. Lett.* 8, 333–336.
914
Booth, J., O’leary, D., Popenoe, P., Danforth, W., 2002. U.S. Atlantic
915 continental slope landslides: their distribution, general attributes,
916 and implications. *U.S. Geol. Surv. Bull.* 14–22.
917
Brooks, T., Johnson, K., 1997. Final report, phase 3 and phase 4 seismic
918 program, Owens Lake, Inyo Country, California, vol. 146.
919
Burger, R.L., Fulthorpe, C.S., Austin Jr., J.A., 2003. Effects of triple
920 junction migration and glacioeustatic cyclicity on evolution of upper
921 slope morphologies, offshore Eel River Basin, Northern California.
922 *Mar. Geol.* 199 (3–4), 307–336.
923
Clarke, S.J., 1987. Geology of the California continental margin north
924 of Cape Mendocino. In: Scholl, D., Grantz, A., Vedder, J. (Eds.),
925 Geology and resources potential of the continental margin of
926 western North America and adjacent ocean basins — Beaufort Sea
927 to Baja California. Earth Science Series. Circum-Pacific Council
928 for Energy and Mineral Resources, vol. 6, pp. 337–351.
929
Constable, C., Tauxe, L., 1990. The bootstrap for magnetic susceptibility
930 tensors. *J. Geophys. Res.* 95, 8383–8395.
931
Couch, R., 1980. Seismicity and crustal structure near the north end of
932 the San Andreas fault system. In: Streitz, R., Sherbourne, R. (Eds.),
933 Studies of the San Andreas Fault Zone in northern California.
934 Special Reports. Calif. Div. Mines Geol., vol. 190, pp. 13–30.
935

- 936 Cronin, M., Tauxe, L., Constable, C., Selkin, P., Pick, T., 2001. Noise
937 in the quiet zone. *Earth Planet. Sci. Lett.* 190 (1–2), 13–30.
- 938 Dillon, W., Lee, M., Fehlhaber, K., Coleman, D., 1993. Gas hydrates
939 on the Atlantic continental margin of the United States — controls
940 on concentration. In: Howell, D. (Ed.), *The future of energy gasses*.
941 US Geological Survey Professional Paper, vol. 1570, pp. 313–330.
- 942 Dodds, D.J., 1980. Attenuation estimates from high resolution
943 subbottom profiler echoes. Saclant Asw Research Conference on
944 Ocean Acoustics Influenced by the Sea floor, vol. 907. Plenum
945 Press, La Spezia, Italy, p. 19.
- 946 Driscoll, N., Diebold, J., 1999. Tectonic and stratigraphic development
947 of the Caribbean: new constraints from multichannel seismic data.
948 In: Mann, P. (Ed.), *Caribbean Basins. Sedimentary Basins of the*
949 *World*, vol. 4. Elsevier Science B.V., Amsterdam, pp. 591–627.
- 950 Driscoll, N.W., Hogg, J.R., 1995. Stratigraphic response to basin
951 formation: Jeanne d'arc basin, off shore Newfoundland. *Geol. Soc.*
952 *Spec. Publ.* 80 (Hydrocarbon Habitat in Rift Basins).
- 953 Egli, R., 2004. Characterization of individual rock magnetic compo-
954 nents by analysis of remanence curves. 3. Bacterial magnetite and
955 natural processes in lakes. *Phys. Chem. Earth* 29 (13–14),
956 869–884.
- 957 Eichhubl, P., Greene, H.G., Maher, N., 2002. Physiography of an
958 active transpressive margin basin: high-resolution bathymetry of
959 the Santa Barbara Basin, Southern California continental border-
960 land. *Mar. Geol.* 184 (1–2), 95–120.
- 961 Embley, R., Jacobi, R., 1986. Mass wasting in the western North
962 Atlantic. In: Vogt, P., Tucholke, B. (Eds.), *The Western North*
963 *Atlantic region*. Vol. M. Boulder Colorado. Geological Society of
964 America, pp. 479–490.
- 965 Evans, D., King, E., Kenyon, N., Brett, C., Wallis, D., 1996. Evidence
966 for long-term instability in the Storegga Slide region off western
967 Norway. *Mar. Geol.* 130, 281–292.
- 968 Field, M., Barber, J., 1993. A submarine landslide associated with
969 shallow sea-floor gas and gas hydrates off northern California. In:
970 Schwab, W., Lee, H., Twitchell, D. (Eds.), *Submarine Landslides:*
971 *Selected Studies in the U.S. Exclusive Economic Zone*. Unites
972 States Geological Survey Bulletin, vol. 2002.
- 973 Fisher, R.A., 1953. Dispersion on a sphere. *Proc. R. Soc. London, Ser.*
974 *A* 217, 295–305.
- 975 Galway, R.S., 2000. The integration of multibeam sonar data with
976 Huntec sub-bottom profile data into a marine GIS. Masters of
977 Science in Engineering. University of New Brunswick.
- 978 Gardner, J., Prior, D., Field, M., 1999. Humboldt Slide — a large shear-
979 dominated retrogressive slope failure. *Mar. Geol.* 154, 323–338.
- 980 Geiss, C.E., Banerjee, S.K., Camill, P., Umbanhowar, C.E., 2004.
981 Sediment-magnetic signature of land-use and drought as recorded in
982 lake sediment from south-central Minnesota, USA. *Quat. Res.* 62 (2),
983 117–125.
- 984 Glen, J., Coe, R., 1997. Paleomagnetism and magnetic susceptibility of
985 Pleistocene sediments from drill hole OL-92, Owens Lake,
986 California. In: Smith, G., Bischoff, J. (Eds.), *An 800,000-year*
987 *Geologic and Climatic record from Owens Lake, California: Core*
988 *OL-92*. Geological Society of America, pp. 67–78.
- 989 Gutowski, M., Bull, J.M., Henstock, T., Dix, J.K., Hogarth, P., Leighton, T.,
990 White, P., 2002. Chirp sub-bottom profiler source signature design and
991 field testing. *Mar. Geophys. Res.* 23 (5–6), 481–492.
- 992 Henkart, P., 2006. Siosies. <http://siosies.ucsd.edu>.
- 993 Hext, G.R., 1963. The estimation of second-order tensors, with related
994 tests and designs. *Biometrika* 50, 353–357.
- 995 Holbrook, W., 2001. Seismic studies of the Blake Ridge: implications
996 for hydrate distribution, methane expulsion, and free gas
997 dynamics. In: Paull, C., Dillon, W. (Eds.), *Natural Gas Hydrates:*
Occurrence, Distribution, and Detection. Geophysical Monograph,
vol. 124. AGU.
- Holbrook, W., Lizarralde, D., Pecher, I., Gorman, A., Hackwith, K.,
Hornbach, M., Saffer, D., 2002. Escape of methane gas through
sediment waves in a large methane hydrate province. *Geology* 30
(5), 467–470.
- Housen, B.A., Kanamatsu, T., 2003. Magnetic fabrics from the Costa
Rica margin: sediment deformation during the initial dewatering
and underplating process. *Earth Planet. Sci. Lett.* 206 (1–2),
215–228.
- Housen, B.A., Richter, C., van der Pluijm, B., 1993. Composite
magnetic anisotropy fabrics: experiments, numerical models, and
implications for the quantification of rock fabrics. *Tectonophysics*
220, 1–12.
- Housen, B.A., Tobin, H., Labaume, P., Leitch, E., Maltman, A., Shipley, T.,
Ogawa, Y., Ashi, J., Blum, P., Bruckman, W., Felice, F., Fisher, A.,
Goldberg, D., Henry, P., Jurado, M., Kastner, M., Laier, T., Meyer, A.,
Moore, J., Moore, G., Peacock, S., Rabaute, A., Steiger, T.,
Underwood, M., Xu, Y., Yin, H., Zheng, Y., Zwart, G., 1996.
Strain decoupling across the decollement of the Barbados accretionary
prism. *Geology* 24 (2), 127–130.
- Hrouda, F., Hruskova, L., 1990. On the detection of weak strain
parallel to the bedding by magnetic anisotropy: a mathematical
model study. *Studia Geophys. Geol.* 34, 327–341.
- Ising, G., 1942. On the magnetic properties of varved clay. *Arkiv. For.*
Mate., Astr., Och Fys. 29, 1–37.
- Kanamatsu, T., Herrero-Bervera, E., Taira, A., 2001. Magnetic fabrics
of soft-sediment folded strata within a Neogene accretionary
complex, the Miura group, central Japan. *Earth Planet. Sci. Lett.*
187 (3–4), 333–343.
- Karlin, R., 1990a. Magnetic mineral diagenesis in suboxic sediments
at Bettis Site W-N, NE Pacific Ocean. *J. Geophys. Res.* 95 (B4),
4421–4436.
- Karlin, R., 1990b. Magnetite diagenesis in marine sediments from the
Oregon continental margin. *J. Geophys. Res.* 95 (B4), 4405–4419.
- King, J., Banerjee, S.K., Marvin, J., Ozdemir, O., 1982. A comparison
of different magnetic methods for determining the relative grain
size of magnetite in natural materials: some results from lake
sediments. *Earth Planet. Sci. Lett.* 59, 44–419.
- King, J., Banerjee, S.K., Marvin, J., 1983. A new rock-magnetic
approach to selecting sediments for geomagnetic paleointensity
studies: application to paleointensity for the last 4000 years.
J. Geophys. Res. 88 (B7), 5911–5921.
- Kopf, A., Berhman, J.H., 1997. Fabric evolution and mechanisms of
diagenesis in fine-grained sediments from the Kita–Yamato
Trough, Japan Sea. *J. Sediment. Res.* 67 (3), 590–600.
- Kumar, A.A., Rao, V.P., Patil, S.K., Kessarkar, P.M., Thamban, M.,
2005. Rock magnetic records of the sediments of the eastern
Arabian sea: evidence for late quaternary climatic change. *Mar.*
Geol. 220 (1–4), 59–82.
- Lee, H.J., Syvitski, J.P.M., Parker, G., Orange, D., Locat, J., Hutton,
E.W.H., Imran, J., 2002. Distinguishing sediment waves from
slope failure deposits: field examples, including the “Humboldt
Slide”, and modelling results. *Mar. Geol.* 192 (1–3), 79–104.
- Leslie, B.W., Hammond, D.E., Berelson, W.M., Lund, S.P., 1990a.
Diagenesis in anoxic sediments from the California continental
borderland and its influence on iron, sulfur, and magnetite
behavior. *J. Geophys. Res.* 95 (B4), 4453–4470.
- Leslie, B.W., Lund, S.P., Hammond, D.E., 1990b. Rock magnetic
evidence for the dissolution and authigenic growth of magnetic
minerals within anoxic marine sediments of the California
continental borderland. *J. Geophys. Res.* 95 (B4), 4437–4452.

- 1060 Liu, J., Zhu, R., Roberts, A.P., Li, S., Chang, J.-H., 2004. High-
1061 resolution analysis of early diagenetic effects on magnetic minerals
1062 in post-middle-Holocene continental shelf sediments from the
1063 Korea Strait. *J. Geophys. Res.* 109 (B03103). doi:10.1029/
1064 2003JB002813.
- 1065 Marino, R., Ellwood, B., 1978. Anomalous magnetic fabric in
1066 sediments which record an apparent geomagnetic field excursion.
1067 *Nature* 274, 581–582.
- 1068 Nittrouer, C., 1999. Strataform: overview of its design and synthesis of
1069 its results. *Mar. Geol.* 154, 3–12.
- 1070 Owens, W.H., 1974. Mathematical model studies on factors affecting
1071 the magnetic anisotropy of deformed rocks. *Tectonophysics* 24,
1072 115–131.
- 1073 Pan, Y., Petersen, N., Davila, A.F., Zhang, L., Winklofer, M., Liu, Q.,
1074 Hanzlik, M., Zhu, R., 2005. The detection of bacterial magnetite in
1075 recent sediments of Lake Chiemsee (southern Germany). *Earth*
1076 *Planet. Sci. Lett.* 232 (1–2), 109–123.
- 1077 Pares, J., van der Pluijm, B., Dinares-Turell, J., 1999. Evolution of
1078 magnetic fabrics during incipient deformation of mudrocks
1079 (Pyreness, northern Spain). *Tectonophysics* 307, 1–14.
- 1080 Pratson, L.F., Coakley, B.J., 1996. A model for the headward erosion of
1081 submarine canyons induced by downslope eroding sediment flows.
1082 *Geol. Soc. Amer. Bull.* 108 (2), 225–234.
- 1083 Quinn, R., Bull, J.M., Dix, J.K., 1998. Optimal processing of marine
1084 high-resolution seismic reflection (chirp) data. *Mar. Geophys. Res.*
1085 20 (1), 13–20.
- 1086 Rees, A.I., 1961. The effect of water currents on the magnetic remanence
1087 and anisotropy of susceptibility of some sediments. *Geophys. J. R.*
1088 *Astron. Soc.* 6, 235–251.
- 1089 Rees, A., 1983. Experiments on the production of transverse grain
1090 alignment in a sheared dispersion. *Sedimentology* 30, 437–448.
- 1091 Rees, A.I., Woodall, W.A., 1975. The magnetic fabric of some laboratory
1092 deposited sediments. *Earth Planet. Sci. Lett.* 25, 121–130.
- 1093 Riedinger, N., Pfeifer, K., Kasten, S., Garmin, J.F.L., Vogt, C., Hensen, C.,
1094 2005. Diagenetic alteration of magnetic signals by anaerobic
1095 oxidation of methane related to a change in sedimentation rate.
1096 *Geochim. Cosmochim. Acta* 69 (16), 4117–4126.
- 1097 Rosenbaum, J., Reynolds, R., Smoot, J., Meyer, R., 2000. Anisotropy of
1098 magnetic susceptibility as a tool for recognizing core deformation:
1099 reevaluation of the paleomagnetic record of Pleistocene sediments
1100 from drill hole OL-92, Owens Lake, California. *Earth Planet. Sci.*
1101 *Lett.* 178, 415–424.
- 1102 Rowan, C.J., Roberts, A.P., 2006. Magnetite dissolution, diachronous
1103 greigite formation, and secondary magnetizations from pyrite
1104 oxidation: unravelling complex magnetizations in Neogene marine
1105 sediments from New Zealand. *Earth Planet. Sci. Lett.* 241 (1–2),
1106 119–137.
- 1107 Schock, S.G., LeBlanc, L.R., Panda, S., 1994. Spatial and temporal
1108 pulse design considerations for a marine sediment classification
1109 sonar. *IEEE J. Oceanic Eng.* 19 (3), 406–415.
- 1110 Schwehr, K., Tauxe, L., 2003. Characterization of soft sediment
1111 deformation: detection of crypto-slumps using magnetic methods.
1112 *Geology* 31 (3), 203–206.
- 1113 Schwehr, K., Tauxe, L., Driscoll, N., Lee, H., in press. Detecting
1114 compaction disequilibrium with anisotropy of magnetic susceptibility.
1115 *Geochem., Geophys., Geosyst.* 7 (1). doi:10.1029/2006GC001378.
- 1116 Sloan, J., Miller, J.R., Lancaster, N., 2001. Response and recovery of
1117 the Eel River, California, and its tributaries to floods in 1955, 1964,
1118 and 1997. *Geomorphology* 36 (3–4), 129–154.
- 1119 Sommerfield, C., Drake, D.E., Wheatcroft, R.A., 2002. Shelf record of
1120 climatic changes in flood magnitude and frequency, north-coastal
1121 California. *Geology* 30 (5), 395–398.
- 1122 Spinelli, G., Field, M., 2001. Evolution of continental slope gullies on
1123 the northern California margin. *J. Sediment. Res.* 71 (2), 237–245.
- 1124 Tarduno, J.A., 1994. Temporal trends of magnetic dissolution in the
1125 pelagic realm: gauging paleoproductivity? *Earth Planet. Sci. Lett.*
1126 123 (1–3), 39–48.
- 1127 Tarling, D.H., Hrouda, F., 1993. *The Magnetic Anisotropy of Rocks.*
1128 Chapman and Hall, London.
- 1129 Tauxe, L., 1998. *Paleomagnetic Principles and Practice.* Kluwer
1130 Academic Publishers.
- 1131 Tauxe, L., Bertram, H., Seberino, C., 2002. Physical interpretation of
1132 hysteresis loops: micromagnetic modelling of fine particle magnetite.
1133 *Geochem. Geophys. Geosyst.* 3 (10). doi:10.1029/2001GC000280.
- 1134 Trincardi, F., Cattaneo, A., Correggiari, A., Ridente, D., 2004. Evidence
1135 of soft sediment deformation, fluid escape, sediment failure and
1136 regional weak layers within the late Quaternary mud deposits of the
1137 Adriatic Sea. *Mar. Geol.* 213 (1–4), 91–119.